

Spatiotemporal Characteristics and Large-Scale Environments of Mesoscale Convective Systems East of the Rocky Mountains

ZHE FENG

Atmospheric Sciences and Global Change Division, Pacific Northwest National Laboratory, Richland, Washington

ROBERT A. HOUZE JR.

*Atmospheric Sciences and Global Change Division, Pacific Northwest National Laboratory, Richland, and
Department of Atmospheric Sciences, University of Washington, Seattle, Washington*

L. RUBY LEUNG, FENGFEI SONG, JOSEPH C. HARDIN, JINGYU WANG, AND WILLIAM I. GUSTAFSON JR.

Atmospheric Sciences and Global Change Division, Pacific Northwest National Laboratory, Richland, Washington


CAMERON R. HOMEYER


School of Meteorology, University of Oklahoma, Norman, Oklahoma

(Manuscript received 19 February 2019, in final form 19 July 2019)

ABSTRACT

The spatiotemporal variability and three-dimensional structures of mesoscale convective systems (MCSs) east of the U.S. Rocky Mountains and their large-scale environments are characterized across all seasons using 13 years of high-resolution radar and satellite observations. Long-lived and intense MCSs account for over 50% of warm season precipitation in the Great Plains and over 40% of cold season precipitation in the southeast. The Great Plains has the strongest MCS seasonal cycle peaking in May–June, whereas in the U.S. southeast MCSs occur year-round. Distinctly different large-scale environments across the seasons have significant impacts on the structure of MCSs. Spring and fall MCSs commonly initiate under strong baroclinic forcing and favorable thermodynamic environments. MCS genesis frequently occurs in the Great Plains near sunset, although convection is not always surface based. Spring MCSs feature both large and deep convection, with a large stratiform rain area and high volume of rainfall. In contrast, summer MCSs often initiate under weak baroclinic forcing, featuring a high pressure ridge with weak low-level convergence acting on the warm, humid air associated with the low-level jet. MCS genesis concentrates east of the Rocky Mountain Front Range and near the southeast coast in the afternoon. The strongest MCS diurnal cycle amplitude extends from the foothills of the Rocky Mountains to the Great Plains. Summer MCSs have the largest and deepest convective features, the smallest stratiform rain area, and the lowest rainfall volume. Last, winter MCSs are characterized by the strongest baroclinic forcing and the largest MCS precipitation features over the southeast. Implications of the findings for climate modeling are discussed.

 Denotes content that is immediately available upon publication as open access.

 Supplemental information related to this paper is available at the Journals Online website: <https://doi.org/10.1175/JCLI-D-19-0137.s1>.

Corresponding author: Zhe Feng, zhe.feng@pnnl.gov

1. Introduction

Deep convection plays a key role in the hydrological cycle and global circulation through redistribution of water and energy in the atmosphere. The largest form of deep convective storms, known as mesoscale convective systems (MCSs), is an ensemble of cumulonimbus clouds that are organized into a storm complex and produce distinct mesoscale circulations (Houze 2004, 2018). MCSs

DOI: 10.1175/JCLI-D-19-0137.1

© 2019 American Meteorological Society. For information regarding reuse of this content and general copyright information, consult the [AMS Copyright Policy \(www.ametsoc.org/PUBSReuseLicenses\)](#).

are commonly observed in the tropics over warm oceans, low-latitude continents (Nesbitt et al. 2006; Yuan and Houze 2010), and midlatitude continents over prominent baroclinic zones (Laing and Fritsch 1997, 2000). They contribute to more than 50% of tropical annual rainfall, and in some regions and seasons over land their rainfall fraction can reach up to 90% (Nesbitt et al. 2006).

In the contiguous United States (CONUS), MCSs play an especially important role in the regional hydrologic cycle and often produce damaging severe weather in the warm season. MCSs contribute to over 50% of the warm season rainfall in large regions of the CONUS, particularly east of the Rocky Mountains (Fritsch et al. 1986; Ashley et al. 2003; Feng et al. 2016; Haberlie and Ashley 2019). MCSs also produce hazardous weather such as damaging hail, tornadoes, lightning, and flooding (Houze et al. 1990; Doswell et al. 1996; Bentley and Sparks 2003; Ashley and Mote 2005; Schumacher and Johnson 2006; Kunkel et al. 2012; Smith et al. 2012; Stevenson and Schumacher 2014). In a warming climate, springtime MCSs in the central United States have become more frequent and produce more intense precipitation in the past 35 years (Feng et al. 2016), and they are projected to further increase and intensify under future warming (Prein et al. 2017b).

MCSs pose a particular challenge to atmospheric modeling due to their multiscale interactions. Convective-scale dynamics are strongly coupled with cloud microphysics through complex hydrometeor phase changes and latent heat release (Varble et al. 2014; Fan et al. 2017). Strong top-heavy diabatic heating produced by MCSs (Schumacher and Houze 2003; Virts and Houze 2015) has significant upscale effects on the large-scale circulations through generation of potential vorticity and enhancement of mesoscale and larger-scale circulations (Chen and Frank 1993; Fritsch et al. 1994; Yang et al. 2017; Feng et al. 2018). A long standing warm and dry bias in the summertime central United States in general circulation models (GCMs) are likely tied to the failure of the models in simulating MCSs and their associated precipitation (Dai et al. 1999; Klein et al. 2006; Lin et al. 2017; Morcrette et al. 2018; Van Weverberg et al. 2018). Convection-permitting models (CPMs) with grid spacing ≤ 4 km have shown promise in simulating the intensity of convective precipitation (Chan et al. 2014; Kendon et al. 2014), the diurnal cycle of precipitation (Ban et al. 2014; Gao et al. 2017), and MCS-like organized precipitation features (Prein et al. 2017a). From limited studies, however, substantial dry bias and underestimation of MCS frequencies still exist in regional convection-permitting simulations over the central United States during summer (Gao et al. 2017; Prein et al. 2017a; Feng et al. 2018). Observational studies have documented various large-scale environment

features important to MCS genesis, such as a low-level jet (LLJ) of air with low static stability and high convective available potential energy (CAPE), a baroclinic frontal zone, vertical wind shear, low-level convergence, and upper-level divergence (Laing and Fritsch 2000; Coniglio et al. 2010; Song et al. 2019). It is unclear if climate models, either global or regional scale, are able to simulate the diverse large-scale environmental conditions that are associated with observed MCSs in different seasons (Song et al. 2019).

Previous studies of MCSs in the United States have mostly focused on the Great Plains during the warm season even though MCSs are also frequently observed outside of that region and in the cool season. Geerts (1998) studied MCSs in the southeastern United States and found a weak seasonal cycle, although small and short-lived MCSs are more common in the summer. Rickenbach et al. (2015) found that MCSs account for 70%–90% of precipitation in the southeastern United States, with a smaller fraction in the summer near the coastal regions. They also reported a lack of MCS diurnal variations except for the southern coastal region during summer. Haberlie and Ashley (2019) examined the seasonal and interannual variability of MCSs using a long-term composite radar reflectivity mosaic images over the eastern CONUS and found that MCS occurrence in the warm season maximizes in the central Plains and Midwest, while cool-season occurrence maximizes in the southeast. What is lacking in previous studies is an examination of the three-dimensional (3D) characteristics of MCSs, which is particularly important in understanding their interactions with the large-scale environment (Schumacher et al. 2004; Feng et al. 2018).

This work aims to characterize the large-scale environments and the associated spatiotemporal MCS characteristics across all seasons in the United States east of the Rocky Mountains. The climatological relationships between atmospheric large-scale environments and 3D MCS characteristics are particularly useful for understanding and modeling the hydrologic cycle and regional climate because MCS activities have large regional and seasonal variability. Taking advantage of modern high-resolution datasets from multiple observing platforms, our goal is to fill the gap in understanding the diurnal, seasonal, and regional variability of MCSs, their 3D structures, and their relationship to and interactions with their large-scale environments. Such information is useful for the climate modeling community as the next generation of high-resolution climate models will increasingly be able to simulate important features of MCSs, thus creating a need for more complete and detailed MCS information to evaluate climate simulations and guide model development.

This paper is organized as follows: [section 2](#) describes the datasets and analysis methods for identifying and tracking MCSs; [section 3](#) presents the seasonal cycle of MCSs; large-scale environments associated with MCSs are examined in [section 4](#); the diurnal cycle of MCSs is provided in [section 5](#); [section 6](#) discusses 3D MCS characteristics; finally, a summary and conclusions are given in [section 7](#). The acronyms used in this study are provided in [Table 1](#).

2. Dataset and analysis methods

a. Observation datasets

In this study, three long-term high-resolution observational datasets are used to obtain various characteristics of MCSs in the United States. Deep convective clouds associated with MCSs are identified using the NASA merged geostationary satellite infrared brightness temperature T_b data ([Janowiak et al. 2001](#)) produced by the National Oceanic and Atmospheric Administration (NOAA) Climate Prediction Center and archived at NASA Goddard Earth Sciences Data and Information Services Center (GES DISC). The 3D MCS characteristics are obtained using a mosaic National Weather Service Next-Generation Radar (NEXRAD) radar reflectivity dataset called GridRad ([Bowman and Homeyer 2017](#)). Precipitation associated with MCSs are obtained using the Stage IV multisensor precipitation dataset produced by the 12 regional forecast centers in the continental United States ([Lin 2011](#)).

The global geostationary satellite T_b dataset not only seamlessly merges all available geostationary meteorological satellites, but also corrects IR temperatures at targets far from satellite nadir where IR temperatures are colder than identical features at a target near satellite nadir ([Janowiak et al. 2001](#)). As a result, the dataset is suitable for quantitative analysis at the regional to global scale, such as tracking deep convective systems in the current study.

The GridRad data are created using a space- and time-weighted binned averaging procedure on a $0.02^\circ \times 0.02^\circ \times 1$ km longitude–latitude–altitude grid. Data from individual NEXRAD radars are binned in GridRad volume out to 300 km from the radar location and within 5 min of the analysis time. All data are weighted during binning using a Gaussian approach that applies greater weights to observations closer in range to the contributing radar location and closer in time to the GridRad analysis time (e.g., 0000 UTC). For more extensive technical detail on the binning and quality control procedures used in the creation and analysis of GridRad data, see [Homeyer and Bowman \(2017\)](#).

TABLE 1. Acronyms used in this study.

Acronyms	Full name
CCS	Cold cloud system
CONUS	Contiguous United States
CSA	Convective–stratiform–anvil classification
ETH	Echo-top heights
FLEXTRKR	Flexible object tracker
LLJ	Low-level jet
MCS	Mesoscale convective system
MSL	Mean sea level
NGP	Northern Great Plains
PF	Precipitation feature
SE	Southeast
SGP	Southern Great Plains
SL3D	Storm labeling in three dimensions classification
T_b	Infrared brightness temperature

The three high-resolution datasets have comparable spatial-temporal resolutions (see [Table 2](#) for details). To create a synthesized dataset for MCS identification and tracking, the GridRad and Stage IV data are regridded onto the satellite 4-km grid using the Earth System Modeling Framework (ESMF) regridding software (<https://www.ncl.ucar.edu/Applications/ESMF.shtml>) and open source Python package xESMF (<https://xesmf.readthedocs.io/>). The GridRad radar reflectivity data are first converted to a linear unit ($\text{mm}^6 \text{m}^{-3}$), then regridded using bilinear interpolation at each vertical level, and finally converted back to a logarithmic unit (dBZ). The Stage IV precipitation data are regridded using the nearest neighbor method since its native resolution is similar to the satellite T_b data. After regridding, a set of quality control software provided by GridRad (<http://gridrad.org/software.html>) was applied to the radar data to remove ground clutter and other nonmeteorological echoes. Visual inspections of the radar data after applying quality control procedures for a selected number of MCS events suggest the GridRad software is effective at 4-km resolution. Weak low-level echoes (radar reflectivity < 10 dBZ below 4-km altitude) were also removed to retain primarily precipitating echoes. Since the objective of this work is to characterize MCSs, removing weak low-level echoes does not have significant impact on our results.

To take advantage of the 3D echo structure provided by the radar data, two radar echo classification methods were applied to the GridRad dataset to obtain convective/stratiform echo types: the convective–stratiform–anvil (CSA) classification ([Feng et al. 2011](#); [Feng et al. 2018](#)) and the storm labeling in three dimensions (SL3D) classification ([Starzec et al. 2017](#)). Both methods primarily use the horizontal texture of radar reflectivity to differentiate convective echoes that have higher peakedness in

TABLE 2. Datasets used in this study, with their resolutions and coverages.

	Spatial resolution	Temporal resolution	Spatial coverage	Temporal coverage
Satellite infrared T_b	~4 km	30 min	180°–180° 60°S–60°N	7 Feb 2002 to current
GridRad reflectivity	~2 km horizontal 1 km vertical	1 h	155°–69°W 25°–49°N	1 Jan 2004 to 31 Dec 2016
Stage IV precipitation	~4 km	1 h	176°–65°W 18°–71°N	1 Jan 2002 to current
NARR	~32 km horizontal 50 hPa vertical	3 h	152°–49°W 1°–57°N	1 Jan 1979 to current

echo intensity compared to the surrounding background. The SL3D also uses the vertical echo structure and melting-layer (0°C) height to better identify intense stratiform rain and weak convective echoes. The melting-layer height was calculated from the 6-hourly ERA-Interim reanalysis (Dee et al. 2011) and linearly interpolated to 1 hourly on the 4-km satellite grid. The major results in this study do not depend on the particular classification method used, suggesting that both methods provide robust characterization of MCS structures in this region. For simplicity, we chose to present results using the SL3D classification method, which was originally designed to take advantage of the GridRad dataset. Contiguous convective echoes were grouped and labeled as convective features. An MCS can have multiple convective features; the largest one at any given time is used to represent the most prominent convective feature, and its 3D characteristics such as size and depth are derived following Feng et al. (2018). Precipitation features (PFs) were defined similarly to convective features: contiguous radar echoes at 2-km height larger than 17 dBZ.

We use the North American Regional Reanalysis dataset (Mesinger et al. 2006) to investigate large-scale environments associated with MCSs. Specifically, we examine geopotential height, zonal and meridional wind, and specific humidity at the convective initiation stage of each tracked MCS. The reason for choosing only the initiation stage is to avoid the substantial feedbacks of MCS heating to large-scale circulations (Yang et al. 2017; Feng et al. 2018) that are potentially imprinted in the reanalysis. For any given MCSs that are initiated within the 3-h window of NARR, the large-scale environments from that 3-h period are selected for analysis.

b. MCS identification and tracking

This study focuses on the 13-yr period from 1 January 2004 to 31 December 2016 when all three high-resolution datasets are available (Table 2). MCSs are identified and tracked using a recently developed

tracking algorithm called the Flexible Object Tracker (FLEXTRKR; Feng et al. 2018). The method first identifies and tracks large cold cloud systems (CCSs; $T_b < 241\text{ K}$) associated with deep convection using satellite T_b data, and subsequently identifies MCSs using radar defined convective features and PFs. Tracking technically runs on satellite-defined CCSs only. A tracked CCS is terminated when no features between two time steps satisfy the 50% area overlap threshold. After a convective system is tracked using satellite-defined CCS, the 3D radar data within the CCS provide better characterization of the evolution of MCS convective features. Because a CCS associated with an MCS can occur before and after the “active” precipitating period (i.e., convective initiation can be detected by satellite T_b signature before precipitation is detected by radar, and the remnants of upper-level clouds can persist for a period after MCS precipitation has ended), we use radar-detected PF rather than satellite-detected CCS to determine the MCS lifetime. Similar to Feng et al. (2018), we focus on long-lived and intense MCSs in this study: an MCS is defined as a large CCS (area $> 6 \times 10^4\text{ km}^2$) containing a PF with major axis length $> 100\text{ km}$, a convective feature containing radar reflectivity $> 45\text{ dBZ}$ at any vertical level, and PF persisting for at least 6 h. Earlier work suggests in order to reach mesoscale circulation in the midlatitude, an MCS should have a length scale of 100 km and last at least 3 h (Parker and Johnson 2000). Most of the recent summaries on MCS climatology based on automated tracking algorithms use a similar convective precipitation feature size criteria, such as major axis length of a feature $> 100\text{ km}$ (although the exact method to define a feature varies significantly in the literature), but the methodologies differ most often in the lifetime criteria, ranging from 2 h (Pinto et al. 2015; Geerts et al. 2017) to 4 h (Geerts 1998; Haberlie and Ashley 2019) to inexplicitly specified values (Prein et al. 2017a). Our selection of MCSs is more stringent in the lifetime criteria because long-lived MCSs have larger impact on the hydrological cycle (Feng et al. 2016) and exhibit

the strongest feedback to the environment (Yang et al. 2017).

A feature update was added to FLEXTRKR in this study to better characterize convective and stratiform echo features and propagation speeds. In close examination of selected MCS cases, we discovered that certain PFs, particularly during the dissipation stage of MCSs when the majority of the MCS consists of stratiform rain area, could be separated into multiple CCSs due to the T_b segmentation procedure in FLEXTRKR. To address this issue, we added additional processing steps during the CCS identification procedure (see Fig. S1 in the online supplemental material): 1) radar reflectivity at 2-km altitude is smoothed using a 5×5 pixel ($\sim 20 \text{ km} \times 20 \text{ km}$) moving window to obtain Z_s (smoothing uses $\text{mm}^6 \text{ m}^{-3}$, which is then converted back to dBZ); 2) a coherent PF is defined as $Z_s > 28 \text{ dBZ}$; and 3) multiple CCSs that share the same coherent PF are grouped as one feature (i.e., CCS-PF-defined MCS). This updated FLEXTRKR algorithm better preserves coherent PFs during all stages of MCSs and therefore provides more accurate statistics of MCS feature size and propagation speed estimates. Nevertheless, because FLEXTRKR uses overlap of the largest CCS between two time steps to determine if they are the same convective system, the tracking is prone to uncertainties in the CCS segmentation procedure. Occasionally the largest overlapping CCS in the next time step belongs to a detaching upper-level anvil cloud from the MCS being tracked, and therefore the tracking would have ended abruptly or appeared to have some spatial “jump.” This tracking failure tends to occur during the decaying stage of MCSs, or when a complicated cluster of multiple MCSs occur near each other. While it is difficult to identify these failures objectively, visual examinations of many tracked MCS events suggest these tracking failures do not occur frequently, and they should not affect the statistical results obtained in this study.

c. Examples of MCSs

An example of a summer MCS in the Great Plains identified by FLEXTRKR is shown in Fig. 1. The long-lived MCS was initiated at 2300 UTC 2 June 2015 near the borders of Wyoming, South Dakota, and Nebraska. It took ~ 5 h for convection to grow upscale into an intense MCS with an arc-shaped convective line. The MCS then continued to propagate southeastward for ~ 1000 km before dissipating at 1900 UTC 3 June 2015 (Fig. 1a). This MCS was initiated ahead of a midlevel trough and upper-level divergence. Nearby soundings at 0000 UTC showed large CAPE near the time of convective initiation, with the low-level temperature inversion eroded at 1200 UTC when an LLJ was established and transporting a large amount of moist and unstable air from the south. Vertical

cross sections showed intense convective echoes of 40+ dBZ reaching above 10 km above mean sea level (MSL) during the initial convective upscale growth stages (Fig. 1b). The MCS maintained a leading convective line/arc and a broad trailing stratiform rain area exceeding $3 \times 10^4 \text{ km}^2$ for ~ 12 h. This intense MCS produced a long swath of accumulated precipitation above 20 mm within 24 h over Nebraska, Kansas, and Missouri (Fig. 1c). The FLEXTRKR algorithm captured the evolution of this MCS very well, as shown by the time series statistics of various MCS properties (Figs. 1d–f). Four life cycle stages were objectively identified based on the convective feature and stratiform rain area characteristics following Feng et al. (2018):

- 1) convective initiation (first hour when a CCS is detected),
- 2) MCS genesis (first hour after the convective feature major axis length reaches 100 km),
- 3) MCS mature (convective feature major axis length remains at 100 km or more, and stratiform rain area $>$ MCS lifetime mean value),
- 4) MCS decay (convective feature major axis length $<$ 100 km or stratiform rain area $<$ MCS lifetime mean value), and
- 5) MCS termination (the major axis length of the largest PF within the CCS $<$ 20 km; i.e., active precipitation of the MCS has terminated).

The convective feature is most intense and largest during the convective initiation and MCS genesis stages, as shown by the deepest convective feature echo-top heights (ETHs) and the largest horizontal dimensions (Figs. 1e,f). An example of a winter MCS in the southeastern United States is discussed in the appendix. While it is unrealistic to investigate each individual MCS identified by FLEXTRKR over the 13-yr period, the authors have selectively examined many individual cases across different years to ensure that the FLEXTRKR algorithm correctly identified MCSs, particularly in the cold seasons. It is found that FLEXTRKR is able to identify a majority of MCSs correctly across all seasons, allowing us to examine their characteristics statistically during the relatively long 13-yr period.

3. MCS seasonal cycle

FLEXTRKR was applied to the 4-km cogridded T_b and GridRad data (section 2a) to track MCSs across all seasons. To facilitate processing time, two separate tracking periods were performed for each year: warm season (March–October) and cold season (November–February). This way the impact from tracking restart (i.e., storms that last through the tracking end time) is

20150602-21Z - 20150603-23Z (Lifetime: 27 h)
2015-06-03 07:00 UTC

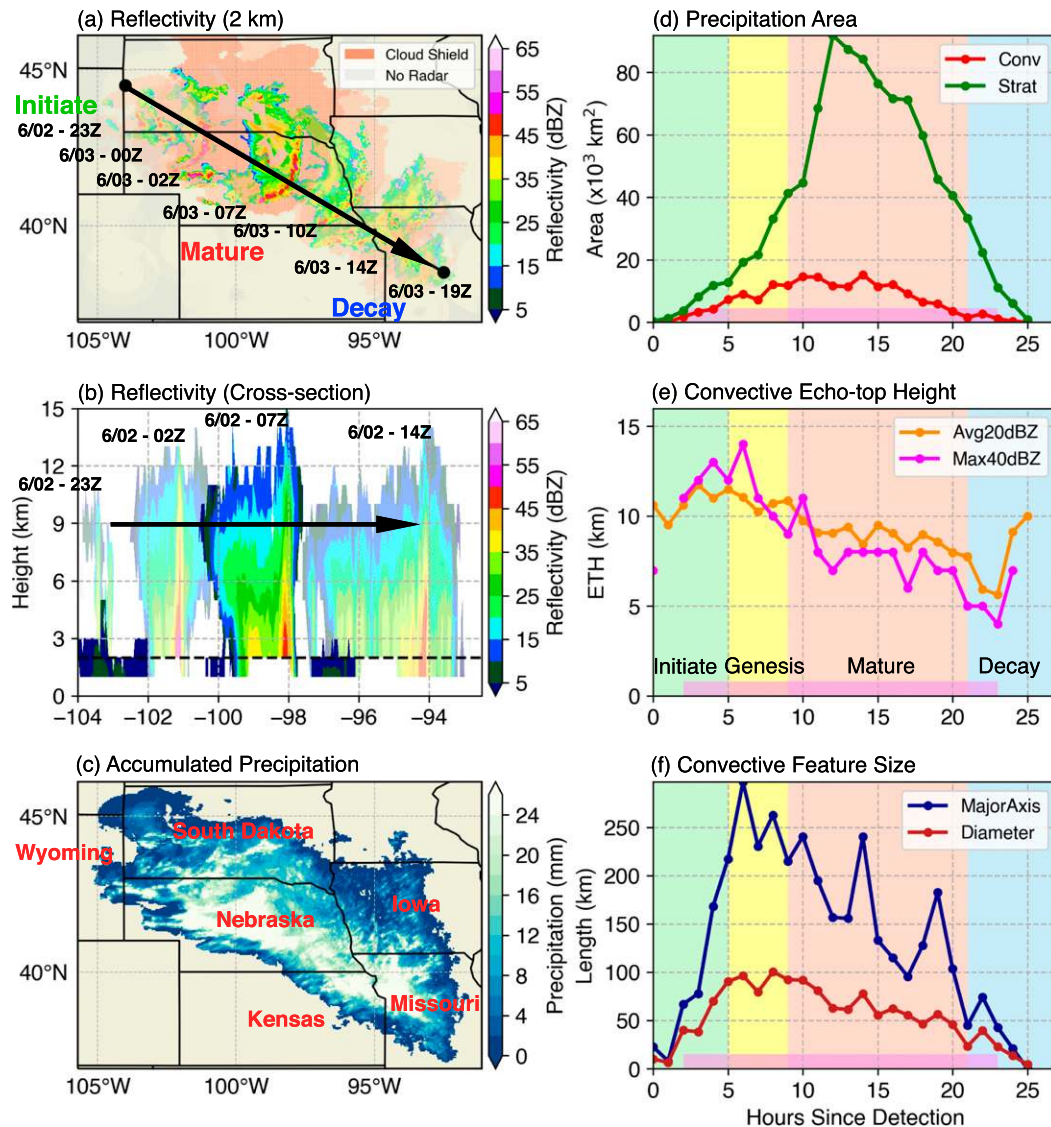


FIG. 1. An example of a summer MCS identified by FLEXTRKR. (a) Snapshots of radar reflectivity at 2-km height MSL at various stages of the MCS, (b) snapshots of radar reflectivity for a vertical cross section along the MCS propagation direction at selected times, (c) accumulated precipitation from this MCS, (d) time series of convective (red) and stratiform (green) precipitation area, (e) time series of convective feature average 20-dBZ ETH (orange) and maximum 40-dBZ ETH, and (f) convective feature major axis length (navy) and equivalent diameter (maroon). The long black arrow in (a) denotes the MCS propagation direction and location of the cross section in (b). The four background color shadings in (d)–(f) indicate the four life cycle stages. The light purple horizontal bar in (d)–(f) denotes when the precipitation feature major axis length > 100 km.

minimized versus more tracking periods. A total of 4646 long-lived and intense MCSs were tracked in the 13-yr period, averaging 357 per year. Some interannual variability of MCS frequency, particularly during the warm seasons, is observed (Figs. S2 and S3). Haberlie and Ashley (2019) examined the interannual variability in more detail using a longer 22-yr MCS record.

Figure 2 shows the spatial distribution of the average number of MCSs for each season (spring: MAM, summer: JJA, fall: SON, winter: DJF). To obtain this map, each 4-km pixel at each hour within the identified MCS that recorded precipitation $> 1 \text{ mm h}^{-1}$ was marked. For the number of MCSs, the entire area where an MCS precipitates $> 1 \text{ mm}$ during its lifetime was counted as

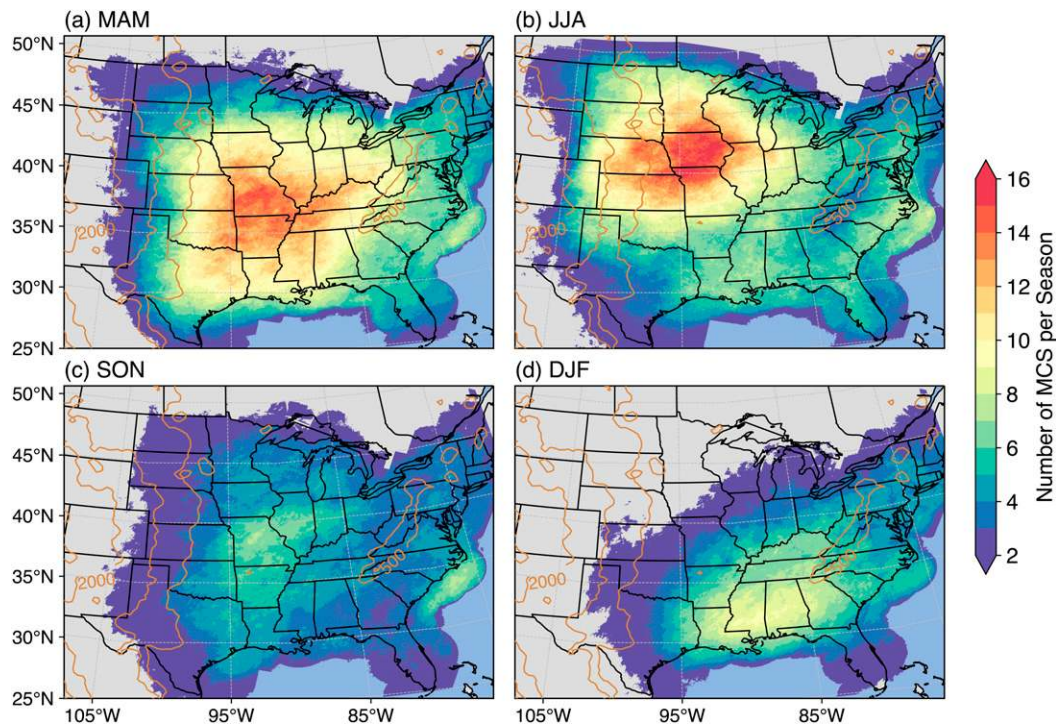


FIG. 2. Spatial distribution of the average number of MCSs during the four seasons for 2004–16: (a) March–May, (b) June–August, (c) September–November, and (d) December–February. Brown contours show the terrain height for 500, 1000, and 2000 m, respectively. Note that areas over the ocean and north of the U.S.–Canada border have reduced radar coverage such that the results in those areas must be treated with caution.

one MCS. All MCS occurrences over 13 seasons were added together and then divided by the total number of seasons (i.e., 13) to obtain the average number of MCSs.

Consistent with previous studies (Haberlie and Ashley 2019), MCSs are most frequent during spring and summer over the central United States (Figs. 2a,b), averaging between 12 and 15 MCSs per season in a large area of the Great Plains. A secondary peak in summer is seen along the southeast coastal states, with a minimum of MCS activity over the Appalachian Mountains (marked by a contour of 500-m terrain height contour oriented southwest to northeast within 85°–75°W, 35°–45°N). Fall has the least number of MCSs, with peak locations similar to those in the spring. MCSs in the winter primarily occur in the southeast United States, averaging about eight per season over the southern coastal states near the Gulf of Mexico.

The spatial distributions of average MCS precipitation fraction and precipitation amount are shown in Fig. 3 and Fig. S4. The spatial distribution of MCS precipitation exhibits a close resemblance to the MCS occurrence (Fig. 2), suggesting that the total MCS precipitation amount at a given location is closely related to the number of MCSs passing through that location. An average of 12–16 MCSs in spring or summer account for

well over 50% of total precipitation over large areas of the Great Plains. In some regions the MCS precipitation fraction can reach up to 70%. These results reaffirm that long-lived and intense MCSs are important to the water cycle in the central United States during the warm seasons. The seasonal and regional contrast in MCS occurrence and contribution to total precipitation found in this study are broadly consistent with previous efforts based on similar NEXRAD network datasets, although details of the tracking methodology and exact definition of MCSs differ somewhat as discussed in section 2b (Geerts 1998; Pinto et al. 2015; Geerts et al. 2017; Prein et al. 2017a; Haberlie and Ashley 2019). Considering that our MCS database only contains long-lived and intense MCSs (lifetime reaching at least 6 h) compared to most previous works (typical lifetime criteria range from 2 to 4 h), this consistency in the MCS precipitation fraction suggests that long-lived and intense MCSs play a major role in the hydrological cycle compared to shorter-lived MCSs. A gradual northward migration of MCS activities from the southern Great Plains (SGP) to the northern Great Plains (NGP) can be seen starting in March and lasting through September (Fig. S5); a westward shift of MCS activity from April to May is also evident. During summer, a reduction of MCS

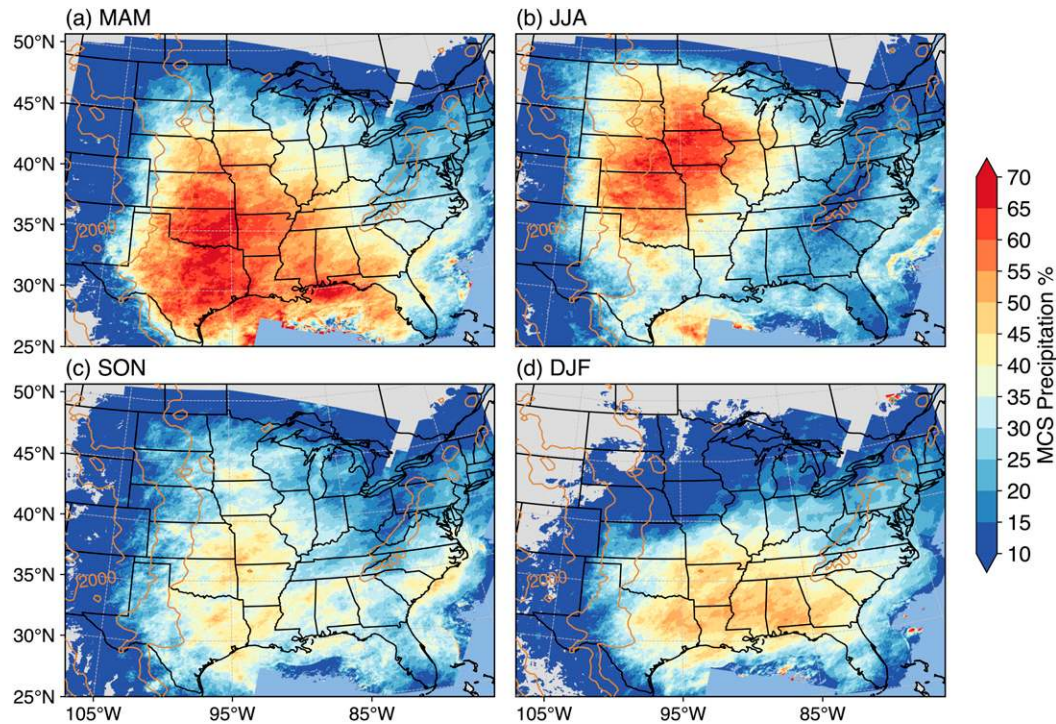


FIG. 3. As in Fig. 2, but for the spatial distribution of the fraction of MCS precipitation for the four seasons from 2004–16.

occurrences in the SGP suggests a shift in the large-scale environments that favor more frequent MCS activities in the NGP. During the cold seasons, particularly in winter, an average of 6–10 MCSs (Fig. 2d) still account for over 40% of the precipitation in the southern states (Fig. 3d). These results suggest MCS properties differ substantially across geographic regions and seasons, which are analyzed further in the subsequent sections.

Based on the spatial distribution of MCS occurrences, we identified three subregions where MCS activities are most frequent east of the Rocky Mountains: 1) NGP, 2) SGP, and 3) the U.S. Southeast (SE). The seasonal cycle of MCS occurrences in these three subregions is shown in Fig. 4. An MCS is designated for occurring in a subregion if the MCS, defined by the center of the MCS PF, spends over half of its lifetime in that subregion. In addition, we excluded MCSs with a lifetime maximum convective feature major axis length < 100 km (i.e., weaker MCSs), because the MCS genesis stage (defined as convective feature major axis length first reaching 100 km) cannot be defined. Only 148 MCSs (or $\sim 3\%$ of the total number of MCS) are excluded by this criterion. A total of 1622, 709, and 588 MCSs were identified for the NGP, SGP, and SE regions, respectively, for subsequent analysis.

Figure 4 shows that the Great Plains have the strongest MCS seasonal cycle. MCSs in the SGP are most

frequent in May (averaging ~ 12) and decrease in the summer as MCS activity shifts northward. NGP MCSs peak in June and remain high during summer (averaging more than 22), but there are rarely any MCSs in the NGP between November and February. The spring season was analyzed extensively from early radar and rain gauge data by Houze et al. (1990). In contrast, MCSs in the SE have a weak seasonal cycle. Although the average number of MCSs in the SE (~ 45) is only $1/4$ of that in the Great Plains (~ 180), MCSs in the SE are more frequent in the cold season. SE MCSs peak in July and December, with a minimum in October. We note that the area of each subregion differs from each other, which affects the number of MCSs in that subregion. In particular, the NGP region is the largest among the three. We tested using a similarly sized domain (12° longitude $\times 8^\circ$ latitude) to study MCSs in the three subregions and the average annual number of MCSs in the NGP decreased to 56 ($\sim 55\%$ reduction) while the other two subregions remain roughly similar. However, the contrast in the seasonal cycle between the three subregions shown in Fig. 4 remains similar; that is, the NGP has the strongest seasonal cycle and the number peaks in June (averaging ~ 13). In addition, MCS characteristics examined in section 6 remain consistent regardless of the exact region selection, suggesting that the MCS regional contrast found in this study is robust. In

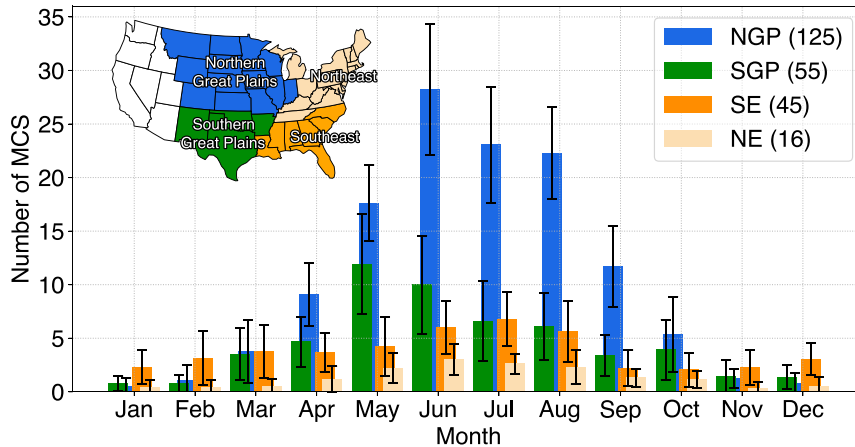


FIG. 4. Monthly average number of MCS occurrences for four regions: 1) northern Great Plains (NGP), 2) southern Great Plains (SGP), 3) U.S. Southeast (SE), and 4) U.S. Northeast (NE). Each region is defined by the states with the same color in the inset. The color bars show the average number, and the error bars show the standard deviation for the 13 years. The numbers in the figure legend are the average number of MCSs in that region per year.

the next section, we examine the large-scale environments associated with MCSs in these three subregions across the four seasons.

4. MCS large-scale environments

In this section, we compare the large-scale environments associated with MCSs in the NGP, SGP, and SE across all four seasons to better understand the key large-scale forcing mechanisms for MCSs in the United States. As described in section 3, the large-scale environments at the convective initiation stage of each of the selected MCSs are included in the composites. Using this point in the MCS life cycle minimizes the potential feedback of the MCS to the large-scale circulations. Figure 5 shows the composite large-scale 925-hPa wind and specific humidity, and 500-hPa geopotential height for the NGP (Figs. 5a–d), SGP (Figs. 5e–h), and SE (Figs. 5i–l) for each season, respectively.

The spring and fall seasons show very similar large-scale environmental patterns, so these seasons are discussed together. Comparing between the three subregions, MCSs in spring/fall tend to initiate under similar synoptic patterns. Convective initiations leading to MCSs commonly occur ahead of a 500-hPa trough associated with baroclinic waves. At 925 hPa, large areas in the Great Plains and scattered areas in the SE exhibit anomalous convergence (Fig. 7); at 200 hPa, each subregion has strong anomalous divergence, with an anomalous upper-level cyclone to the west and an anomalous anticyclone to the east (Fig. 8). The low-level convergence and upper-level divergence suggest deep large-scale lifting occurs ahead of the trough, providing a more

favorable large-scale environment (e.g., maintaining a high relative humidity in the low to middle troposphere) for upscale growth and maintenance of deep convection. This pattern is consistent with the findings by Song et al. (2019), who identified several types of large-scale environments associated with MCSs to be dynamically favorable for maintaining convection. Ahead of the trough, the Great Plains low-level jet is likely enhanced by the passage of baroclinic waves. The LLJ transports large amounts of warm and moist air into the subregions, leading to instabilities needed for MCS upscale growth. Moisture and wind anomalies at 925 hPa are larger over the NGP than the SGP and SE, suggesting that a stronger low-level moisture flux is needed at higher latitudes where low-level temperature and instability alone may be insufficient to support MCS development in spring/fall.

Given the similarities in the composite large-scale environments between spring and fall, one may ask why MCSs are less frequent in the fall than in the spring (Fig. 2). The composite environment results only show the large-scale circulation patterns leading to MCS occurrence, not how often these circulation patterns occur. A possible explanation for less frequent MCSs in the fall is that surface temperatures, particularly over high latitudes, are much warmer in the fall season following the summer, compared to the spring season which follows the winter (not shown). The reduced temperature gradient with latitudes in the fall means less frequent and potentially weaker baroclinic waves, and hence MCS occurrence frequency is much lower in the fall season.

The large-scale environments associated with summer MCSs are shown in Figs. 5b,f,j, 6b,f,j, 7b,f,j, and 8b,f,j. The summer season environments differ substantially

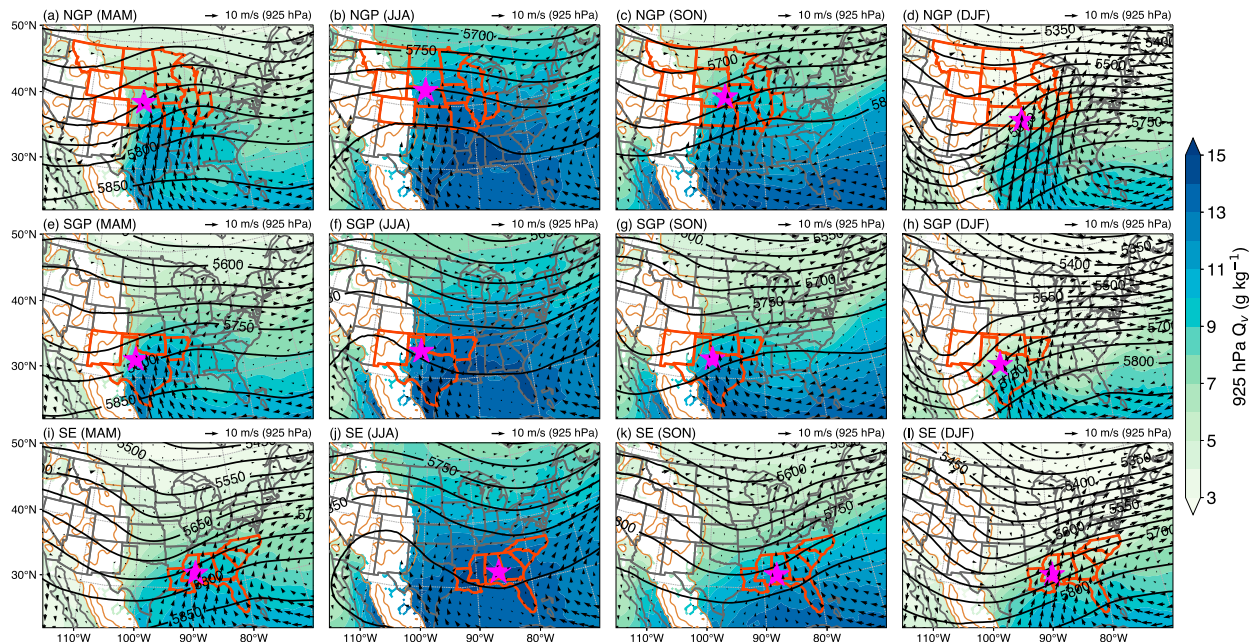


FIG. 5. Composite large-scale environments for each season (by column) for MCSs in the (a)–(d) NGP, (e)–(h) SGP, and (i)–(l) SE regions. Shadings are 925-hPa specific humidity, vectors are 925-hPa wind, and black contours are 500-hPa geopotential height. Terrain heights are in brown contours (1000 and 2000 m). The analysis regions are marked with orange outlines. Note that only the convective initiation stage for each MCS is included in the composite (see text for more details). The averaged centroid locations of MCS convective initiation in each region are shown by the star.

from spring and fall. The majority of CONUS is occupied by a high pressure ridge, the low-level ridge is partly associated with the westward extension of the North Atlantic subtropical high (Li et al. 2012), and the upper-level ridge is partly influenced by the subtropical ridge associated with the North American monsoon (Higgins et al. 1997). The three subregions are either dominated by a ridge or just east of a ridge. At 925 hPa, an area of weak anomalous convergence is seen just east of the Rocky Mountains. The divergence at 200 hPa is also the weakest among all seasons (Figs. 8b,f,j), suggesting that the large-scale rising motion is weak or limited. In comparison, the mean 925-hPa humidity is the highest among all seasons due to warmer temperatures in the summer, but the humidity anomalies are rather small for all subregions. These features suggest that smaller-scale disturbances acting on the abundant mean-state moisture in the summer may be sufficient to support MCS development in the absence of large-scale dynamical forcing. For example, strong diurnal heating near the Rocky Mountains foothills, or sea breeze convergence near the SE coastal region during daytime, can provide triggering mechanisms for local convection. Upscale growth of local afternoon convection into MCSs requires additional forcing support. Wang et al. (2011a,b) found that under northwesterly flow associated with the

high pressure ridge, midtroposphere (~ 600 hPa) short-wave perturbations are frequently generated over the Rocky Mountains in the NGP summer and propagate southeastward downstream with the background flow. Such midtroposphere disturbances have preferred diurnal timing (Wang et al. 2011b); when the disturbance collocates with sufficient low-level moisture and instability provided by the nocturnal LLJ, MCS genesis can occur over the NGP (Wang et al. 2011a). It should also be pointed out that here we focused on the averaged large-scale environment associated with MCS. Song et al. (2019) found that even in the summer, there are also considerable percentages of MCSs associated with large-scale favorable environments similar to spring. Moreover, Song et al. (2019) showed that for MCSs that develop under unfavorable large-scale environments, sub-synoptic-scale rising motions could be associated with these midtropospheric perturbations or local-scale circulations. These small-scale perturbations are likely more important for triggering MCSs in the summer than the large-scale environments, but the perturbations would be difficult to reveal in large-scale composite analyses that only reveal the mean conditions.

Large-scale environments associated with winter MCSs are shown in Figs. 5d,h,l, 6d,h,l, and 7d,h,l. In contrast to the summer season, winter exhibits the strongest

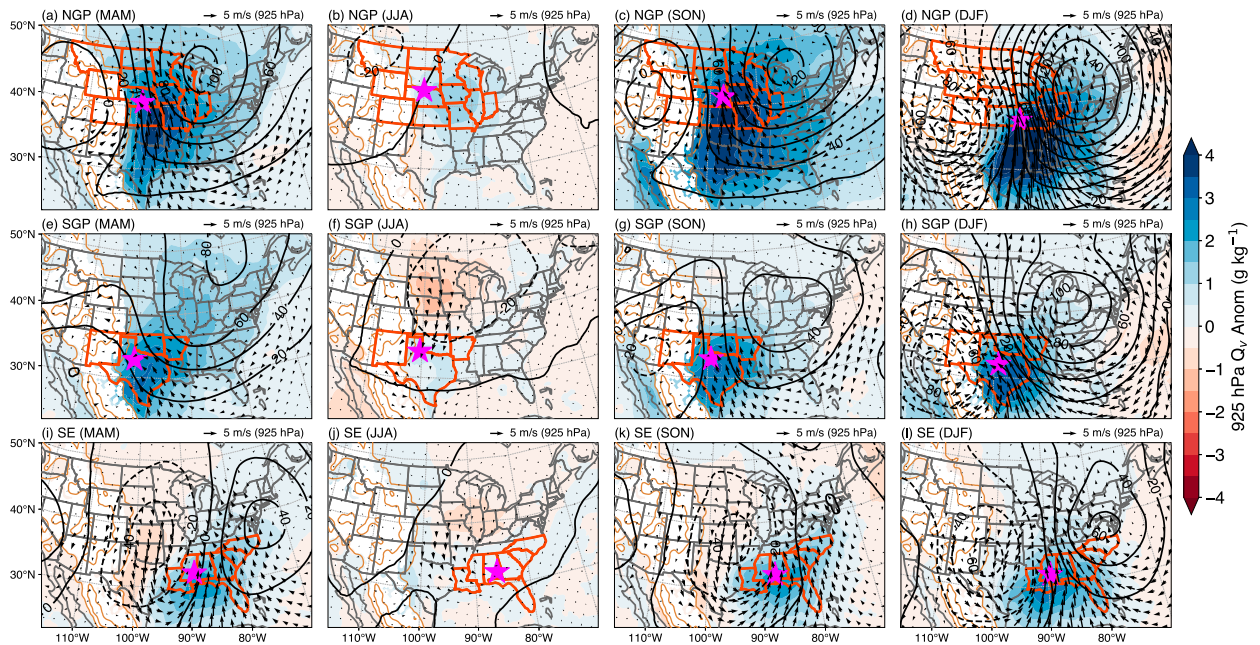


FIG. 6. As in Fig. 5, but for anomalies. The anomaly fields are calculated by subtracting the 13-yr seasonal mean from the mean during the MCS initiation stage.

synoptic forcing associated with baroclinic waves. The mean low-level moisture is small and confined to the SE. During the passage of strong baroclinic waves, as depicted by tight gradients and large anomalies in the 500-hPa geopotential height, large moisture anomalies and convergence are seen at 925 hPa, along with the

strongest 200-hPa divergence (Figs. 8d,h,l). Large, positive moisture anomalies primarily occur in the SGP and the SE and extend partially to the southeastern region of the NGP. This is consistent with the limited winter MCS activity in the NGP (Fig. 2d). These results suggest that in the winter, the strongest baroclinic forcing of any season

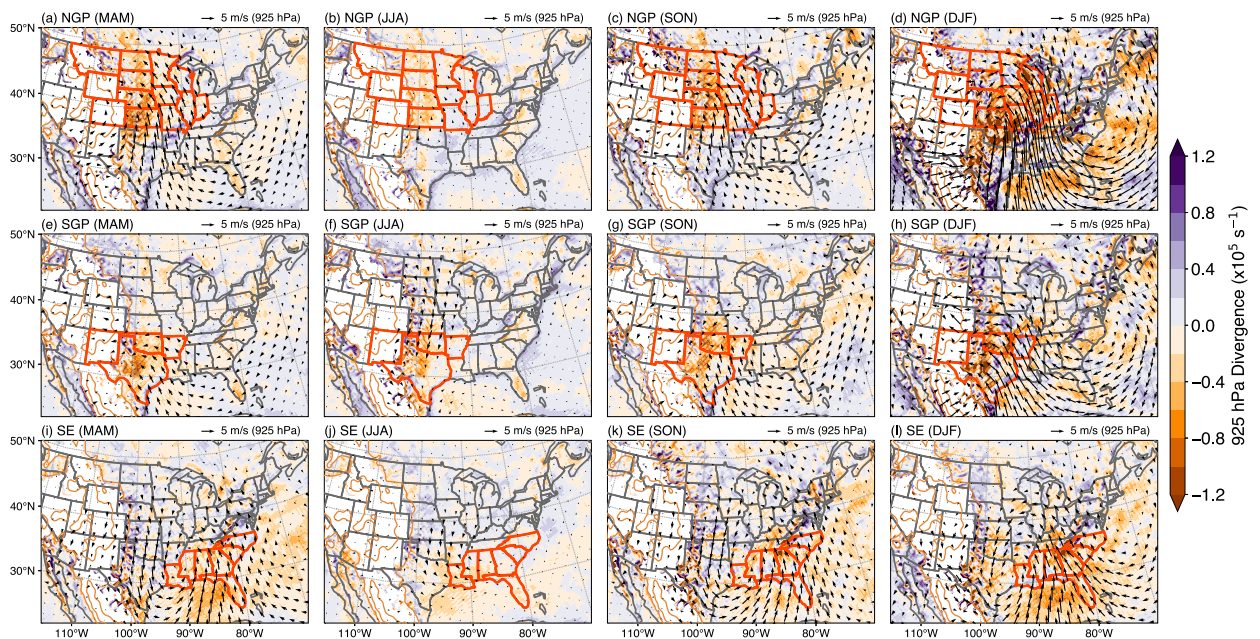


FIG. 7. As in Fig. 6, but the shading denotes 925-hPa divergence.

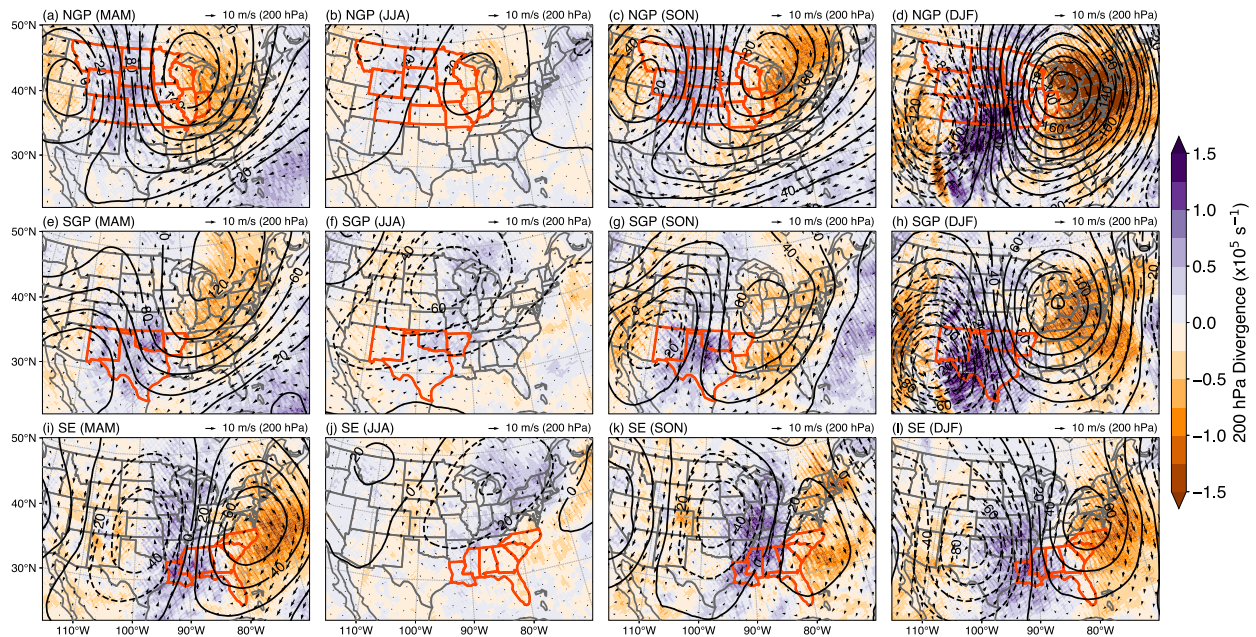


FIG. 8. As in Fig. 6, but for 200-hPa divergence.

is needed to overcome the unfavorable thermodynamic environments in the lower troposphere (i.e., cooler and drier) to support MCS developments in the southern United States.

5. MCS diurnal cycle

Here we examine the MCS diurnal cycle across the four seasons in relation to the large-scale environment analysis in the last section to better understand the mechanisms for MCS initiation. The spatial distributions of MCS genesis location during the four seasons are shown in Fig. 9. Note that MCS genesis is defined to occur after the convective feature major axis length first reaches 100 km. The MCS samples plotted in Fig. 9 are similar to those of Fig. 2, with one key difference: MCSs that are part of a split from a pre-existing MCS are excluded in Fig. 9. Therefore, this map shows MCSs that grow naturally without complex storm splitting processes. At the time of a given MCS that reaches the genesis stage, the MCS PF is marked on the map, and then aggregates over time to obtain the results shown in Fig. 9.

During spring, the most frequent MCS genesis locations are in the central Great Plains (Kansas, Missouri, Oklahoma, Arkansas, Texas) and near the southern coastal states (Mississippi, Alabama). The preferred MCS genesis locations are consistent with the favorable large-scale environments that provide both dynamical and thermodynamical supports in those regions during

spring. In summer, MCS genesis is much more concentrated just east of the Front Range of the Rocky Mountains in the eastern Colorado plains, western Nebraska, and Kansas. Secondary peak locations are over Iowa, Missouri, and along the coastal area of the SE states. As discussed in section 4, the strong diurnal heating over the Rocky Mountains in the local afternoon, coupled with sub-synoptic-scale disturbances acting on the abundant low-level moisture may be important mechanisms for triggering MCSs over the Front Range. Carbone and Tuttle (2008) showed that the afternoon triggering and genesis of summer MCSs on the lee side of the Rocky Mountains and their subsequent eastward propagations into the Great Plains in the nocturnal hours are likely associated with the mountain-plains solenoidal circulation, which is a thermally driven circulation associated with the differential cooling rates between mountains and plains. On the other hand, Tuttle and Davis (2006) found that during July and August, a stronger Great Plains LLJ favors greater percentage of locally forced MCSs triggered over the Great Plains compared to those propagated from the Rocky Mountains, resulting in increased precipitation amount in the plains. More recently, Song et al. (2019) found two types of synoptically favorable MCS environments in summer that have frontal characteristics and an enhanced LLJ similar to spring, and two types of unfavorable environments with an enhanced upper-level ridge, similar to those found in this study (Figs. 5b,f). MCS genesis in the summer over the Great

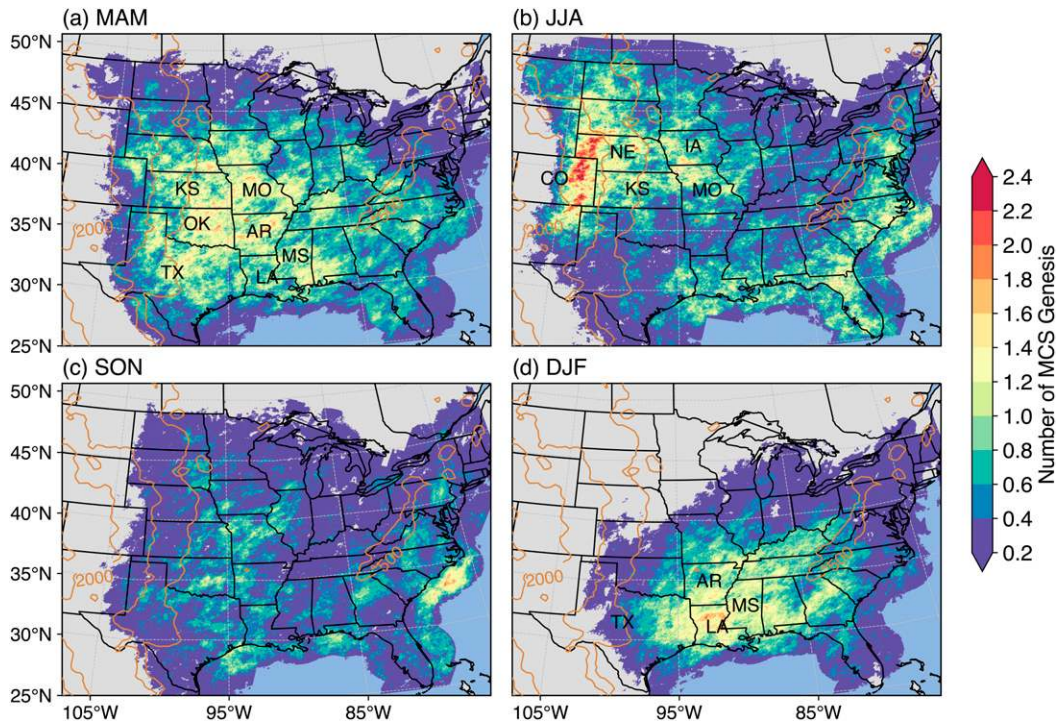


FIG. 9. Spatial distribution of the average number of occurrences of MCS genesis for the four seasons from 2004 to 2016. MCS genesis is defined as when the convective feature major axis length first reaches 100 km. Note that MCSs that originate from an MCS split are excluded from the analysis. State name abbreviations: Alabama (AL), Arkansas (AR), Colorado (CO), Iowa (IA), Kansas (KS), Louisiana (LA), Mississippi (MS), Nebraska (NE), Oklahoma (OK), Texas (TX).

Plains under unfavorable large-scale environments poses a significant challenge for coarse-resolution models because the mesoscale and small-scale disturbances important for triggering MCSs are likely under resolved or misrepresented. The secondary MCS genesis areas along the coastal states of the SE are likely associated with sea breeze convergence from strong diurnal heating in the local afternoon.

Similar to spring, MCS genesis locations in fall are primarily over the central Great Plains, but the frequency is lower. The preferred locations are consistent with the similarity in large-scale environments between fall and spring. During winter, MCS genesis most frequently occurs over the tristate area of Louisiana, Arkansas, and Mississippi, consistent with the strongest low-level moisture anomalies associated with winter baroclinic waves over that region.

The diurnal cycles of convective initiation and MCS genesis for the four seasons are shown in Fig. 10. To quantify the diurnal cycle, a Fourier transform was applied to the diurnal cycle of the number of MCSs, and the first harmonic of the signal with a 24-h period was used (Wallace 1975). The amplitude and phase of the first harmonic of the diurnal cycle represents the strength of

the diurnal cycle and the peak timing, respectively, while the percent variance explained by the first harmonic denotes how well the diurnal cycle is represented by a sine wave (Gustafson et al. 2014). MCSs in the NGP generally have the strongest diurnal cycle across the three regions during all seasons except winter. In contrast, MCSs in the SE have the weakest diurnal cycle except summer.

Compared to spring and fall, summer has the most distinct diurnal cycle, as evidenced by the highest percent variance explained by the first harmonic. Most of the convective initiation in the Great Plains occurs in the early local afternoon (1300–1500 LST; Fig. 10c). Isolated convection typically takes 3–4 h to organize into MCSs, which peak around sunset (1800–1900 LST; Fig. 10d). In the SE, convective initiation peaks much earlier at 10 LST, and MCS genesis peaks in early local afternoon (1300 LST), which is 4–5 h earlier than the Great Plains. As noted in section 5, strong diurnal heating and small-scale perturbations are likely more important than large-scale environments in triggering summer MCSs, as suggested by the large-scale subsidence associated with the high-pressure ridge and abundant low-level moisture (Fig. 5). Consistent with the large-scale environment analysis, we find that the majority of summer

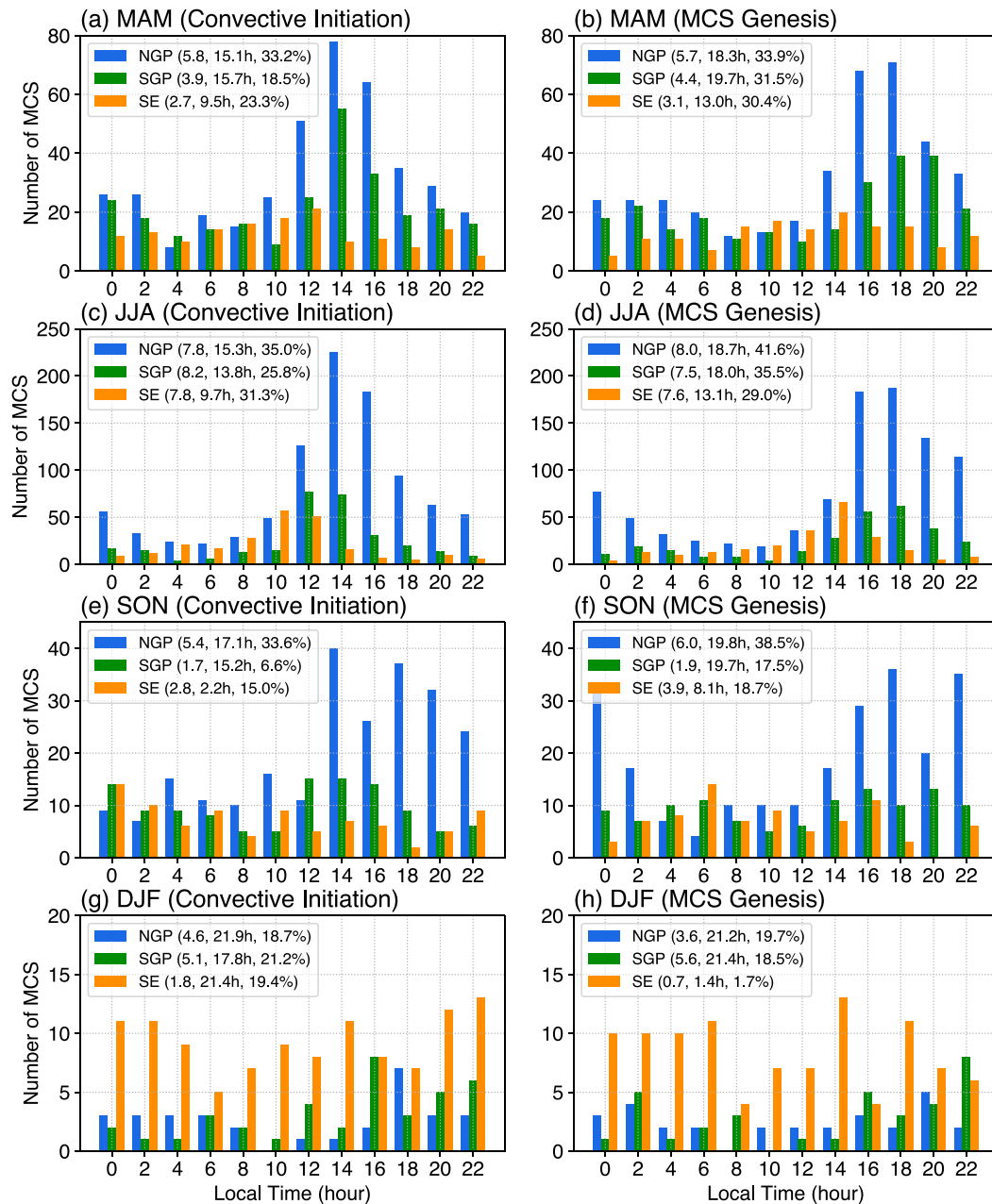


FIG. 10. Diurnal cycle of the number of occurrences of (left) MCS convective initiation and (right) MCS genesis for the three subregions and four seasons: (a),(b) MAM, (c),(d) JJA, (e),(f) SON, and (g),(h) DJF. Numbers in the legends are the amplitude (normalized unitless), phase (peak timing), and percent variance explained for the first harmonic of the diurnal cycle, respectively, in each subregion and season. The amplitude of the first harmonic is calculated using the normalized frequency of MCS in each region, such that it is comparable across regions and seasons.

MCSs were triggered in the afternoon in phase with the diurnal heating, resulting in the strongest diurnal cycle amplitude.

In contrast to summer, spring and fall MCSs in the Great Plains show a weaker diurnal amplitude (Figs. 10a,b,e,f), with relatively more MCSs triggering

in the nocturnal and early morning hours (0000–0800 LST). More frequent passage of baroclinic waves in spring and fall provides favorable large-scale lifting and low-level moisture anomalies (Figs. 5 and 6) that can trigger MCSs outside of the local afternoon hours. In the SGP where MCS activity peaks during late spring, a

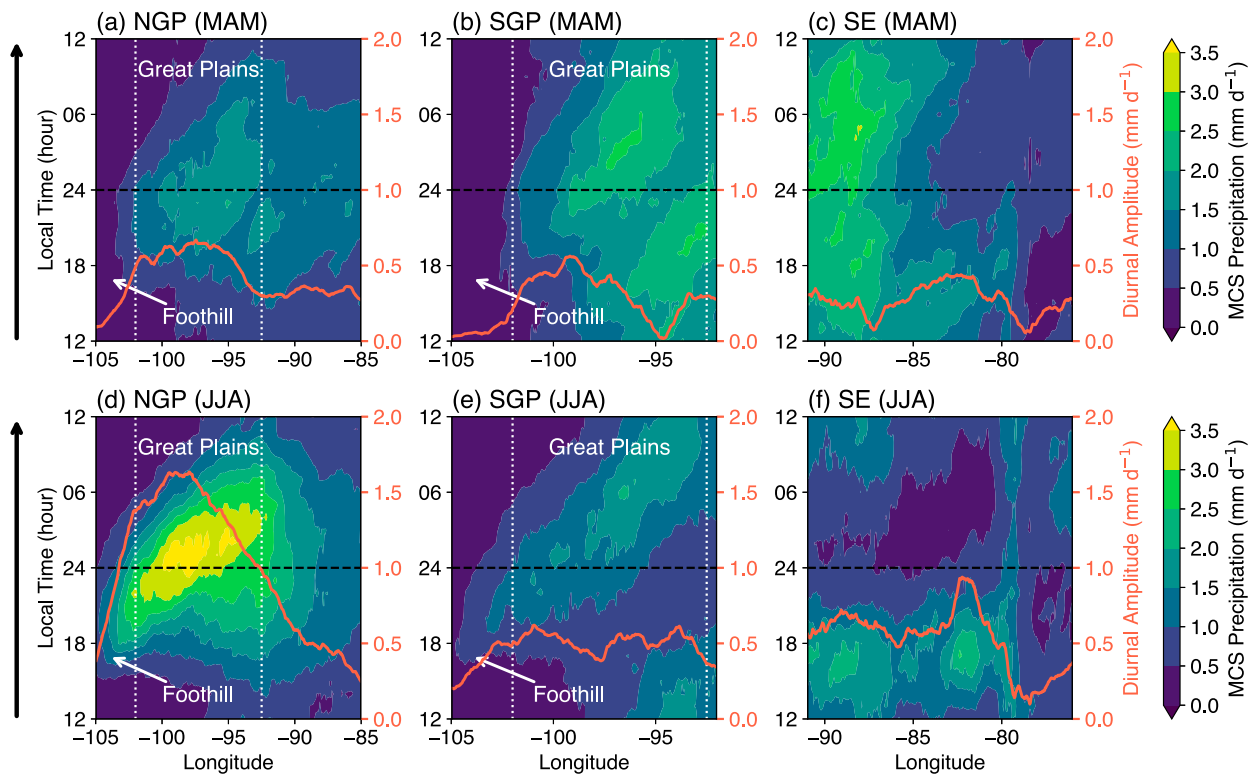


FIG. 11. Diurnal cycle of MCS precipitation as a function of longitude for the three subregions during (top) spring and (bottom) summer. MCS precipitation is averaged in the latitude dimension over each subregion defined in Fig. 4. Orange lines show the first harmonic of the diurnal cycle composite amplitude along each longitude. Approximate locations of the Rocky Mountain foothill and the Great Plains are marked.

climatological feature known as the dryline (Fujita 1958; Schaefer 1974; Hoch and Markowski 2005) often favors convective storm initiation along the strong moisture gradient boundary. Passage of baroclinic waves or frontal systems can enhance the low-level wind convergence and moisture gradient near the dryline, pushing the moist air east of the dryline upward to allow potential instability to be released and initiate convection (Fujita 1958; Ziegler et al. 1997). Such processes can occur at any time of the day, irrespective of the surface conditions. Therefore, the diurnally forced local convection plays a relatively smaller role in MCS genesis during spring and fall compared to the summer.

MCS initiation during winter shows little to no diurnal cycle (Figs. 10g,h), particularly in the SE, where MCSs are largely controlled by strong baroclinic waves and synoptic frontal systems. The weak MCS diurnal cycle in the SE during cold seasons is consistent with previous work by Geerts (1998). MCS occurrences in the Great Plains are rather low during winter.

To further examine the zonal difference of the MCS diurnal cycle, we selected the spring and summer seasons when MCSs are most frequent and display the

strongest diurnal cycle. The composite diurnal cycle of MCS precipitation as a function of longitude for the three subregions is shown in Fig. 11. Eastward propagation of the MCS precipitation during the day is clear in the Great Plains for both spring and summer. In the SE, spring MCSs seem to be a continuation of MCSs propagating from the SGP; in summer, there is no obvious eastward propagation and instead, the diurnal cycle has a maximum that anchors in the late afternoon and dissipates in early evening, which is in sharp contrast with MCS behavior in the Great Plains.

During spring, MCS precipitation in both the SGP and the NGP peaks around local midnight or early morning, with some evidence of initiation in late afternoon just east of 100°W , consistent with Fig. 10b. Compared to the NGP, the amplitude of the MCS precipitation diurnal cycle for the SGP is slightly lower ($\sim 95^{\circ}\text{W}$), due to more MCS precipitation in the late morning and early afternoon hours. During summer, the diurnal cycle amplitude of the MCS precipitation increases significantly around the Rocky Mountains foothill (due west of 100°W). Consistent with Figs. 10d and 9b, MCS precipitation clearly initiates during late afternoon, and

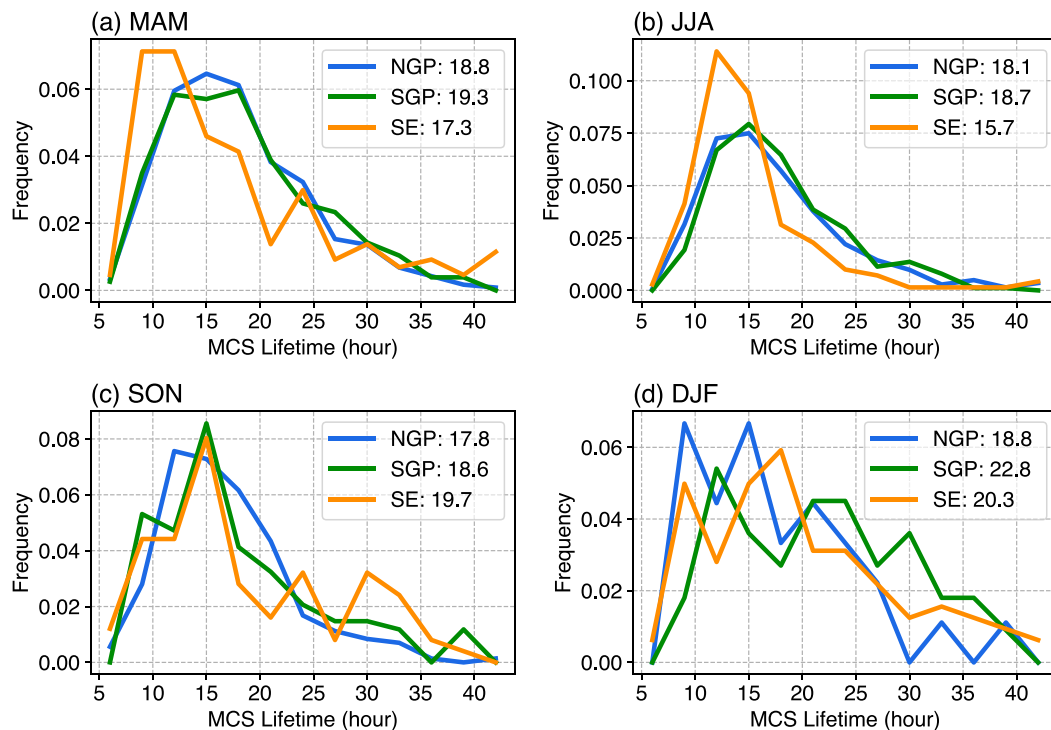


FIG. 12. Frequency distribution of MCS lifetime for the three subregions during the four seasons. Numbers in the legends are the average lifetime lengths (h) in each subregion and season.

much closer to the Rocky Mountains Front Range ($\sim 105^{\circ}\text{W}$) where the terrain has the sharpest gradient. The strongest summer MCS precipitation diurnal cycle amplitude is observed over much of the NGP region, spanning between 105° and 90°W . The eastward propagating summer MCS diurnal cycles over the Great Plains shown in Fig. 11 are very similar to the Hovmöller diagrams of coherent precipitation episodes shown by Carbone and Tuttle (2008) (their Figs. 5 and 6), suggesting that MCSs make major contributions to the intense coherent precipitation episodes during summer over this region. Our results confirm that MCSs make primary contributions to the observed nocturnal peak precipitation and previously reported intense coherent precipitation episodes in the Great Plains during the warm season reported in many previous studies (Wallace 1975; Balling 1985; Dai et al. 1999; Carbone et al. 2002; Jiang et al. 2006; Carbone and Tuttle 2008).

6. MCS characteristics from 3D radar data

In this section, we present seasonal MCS characteristics, derived primarily from the unique 3D radar dataset covering a large region of the CONUS, to better understand the influence of large-scale environments to MCS structures and evolution.

Figure 12 shows the frequency distribution of MCS lifetime by season over the three subregions. MCS lifetime in this study is defined as the period when any PF major axis length within the tracked CCS exceeds 20 km. Therefore, the MCS lifetime represents the period when the MCS is actively producing precipitation, which is usually shorter than the MCS cloud lifetime derived from satellite. During spring and summer, MCSs in the Great Plains typically last between 10 and 24 h, with a mode around 15 h. In contrast, MCSs in the SE are shorter lived. They mostly last less than 20 h, with a mode around 10–12 h. During fall and winter, the regional difference is smaller with an average MCS lifetime around 18–20 h.

The spatial distribution of average MCS propagation speed is shown in Fig. 13. The propagation speed is calculated using a 2D cross-correlation map between two consecutive hours of the MCS PFs, as detailed in Feng et al. (2018). Because radar reflectivity within the PFs is used to calculate the 2D cross-correlation map, the estimated propagation speed should represent the motion of the broader MCS rather than the embedded convective elements, which in some cases (e.g., convective “training” events) could propagate at speeds different from that of the broader MCS. MCS propagation speed for each time interval is mapped onto the

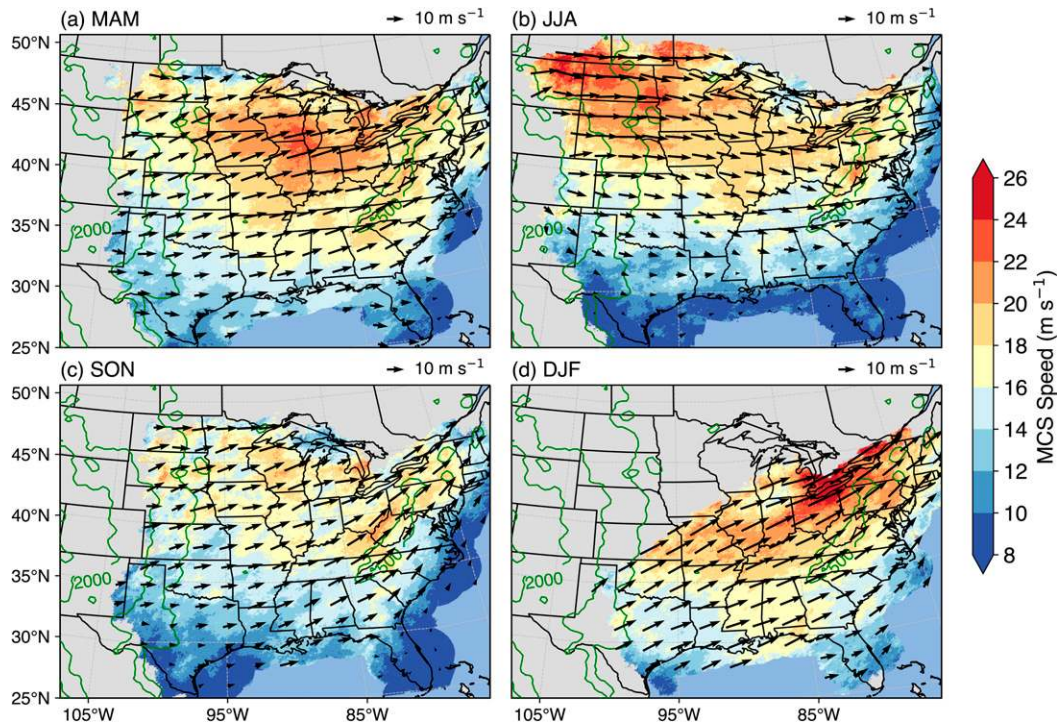


FIG. 13. Spatial distribution of the average MCS propagation speed for each season from 2004 to 2016. Shadings denote the propagation speed at the native 4-km resolution, and vectors show the propagation directions. Terrain heights are in green contours (500, 1000, and 2000 m).

MCS PF (4-km resolution) and subsequently averaged across all MCSs within a season to obtain the results in Fig. 13. The average MCS propagation direction varies considerably across the four seasons, but the direction generally follows the average midtropospheric wind direction (i.e., along the 500-hPa geopotential height contours shown in Fig. 5). For example, the spring and fall season MCSs in the Great Plains tend to propagate northeastward ahead of the midlevel trough (Figs. 5a,c,e,g); summer MCSs tend to propagate eastward in the NGP and gradually change to southeastward over the Great Lakes region downwind of the high pressure ridge (Figs. 5b,f). The alignment of the MCS propagation direction and midtropospheric wind direction is likely related to the momentum transport by the MCS mesoscale downdraft (Moncrieff 1992).

MCSs in the NGP tend to have faster propagation speeds across all seasons compared to the other two subregions. The average MCS propagation speed is between 18 and 20 m s^{-1} in the NGP, with most MCSs propagating between 6 and 30 m s^{-1} (Fig. S6). The faster propagation speed for NGP MCSs probably reflects the MCSs mesoscale downward transport of air with stronger zonal wind velocity in the more northern location. These results are consistent with the 7–30 m s^{-1} zonal

phase speed of the warm season heavy precipitation episodes reported by Carbone et al. (2002). During summer, when the baroclinic forcing is weak (Figs. 5 and 6), other mechanisms such as gravity waves (Tripoli and Cotton 1989) and density current propagating in the planetary boundary layer could trigger new MCSs and result in discrete propagation (Carbone et al. 1990), possibly enhancing the MCS propagation speeds. During spring, stronger lower-to-middle tropospheric wind associated with baroclinic forcing enhances the MCS propagation speed in the southern region, making it more similar to that in the NGP. MCS propagation speeds during fall is similar to summer, except the NGP MCSs are slightly slower. Finally, winter MCSs have comparable propagation speeds as they are all associated with the strongest baroclinic forcing.

The spatial distribution of average MCS PF equivalent diameter ($D = \sqrt{4\text{Area}/\pi}$) is shown in Fig. 14. Strong seasonal and regional variations are observed in the size of MCS PF. Summer has the smallest MCS PF, where the NGP shows moderate MCS PF around 300–350 km. A region with minimum MCS PF size separates the NGP from the coastal region of the SE, where MCS PFs have comparable size with the NGP. The limited size of summer MCS PFs is likely explained by the weak

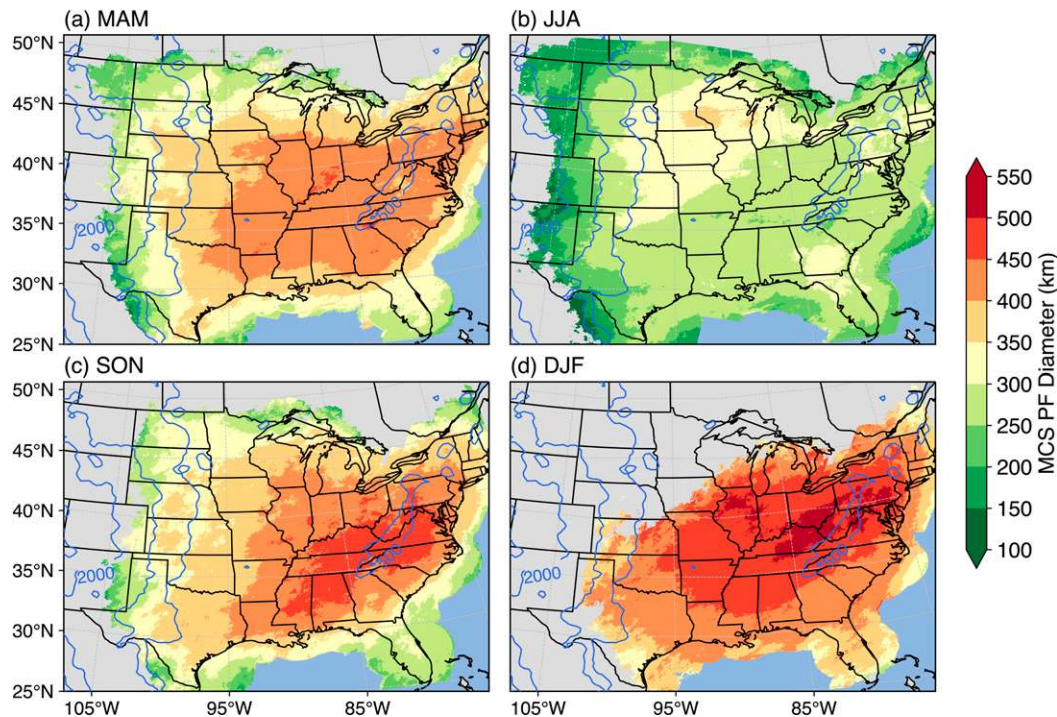


FIG. 14. Spatial distribution of the average MCS precipitation feature (PF) equivalent diameter for each season from 2004 to 2016. Terrain heights are in blue contours (500, 1000, and 2000 m).

or limited large-scale rising motion during summer (section 4). Spring and fall seasons have comparably larger MCS PFs than summer, generally reaching 400–450 km in the central and eastern United States. MCS PFs are noticeably larger east of the Great Plains over the Appalachian Mountains and the southeast. Larger MCS PFs, primarily in the form of stratiform precipitation (discussed in more detail next), is consistent with deep large-scale lifting motion associated with southwest-to-northeast oriented baroclinic waves and enhanced low-level moisture transport via the LLJ (Fig. 5). Finally, MCS PFs are largest during winter, exceeding 450 km in many places. These MCSs are supported by the strongest baroclinic waves and synoptic fronts. The sharp contrast in MCS PF size between winter and summer, particularly in the SE, is consistent with the previous study by Geerts (1998).

The spatial distributions of average MCS convective feature equivalent diameter and 20-dBZ ETHs are shown in Figs. 15 and 16, respectively. A striking contrast is seen for MCS convective feature 3D characteristics compared to MCS PFs. Summer MCS convective features are largest and deepest, particularly over the NGP. The average MCS convective feature equivalent diameters exceed 80 km over much of the NGP, and the average 20-dBZ ETH reaches well above 8 km in altitude (MSL), suggesting that the strongest convective updrafts are

lofting large ice particles high in the upper troposphere and producing large areas of intense convective precipitation. The convective features are deeper (reaching 10 km or above) on average over the MCS initiation region closer to the Rocky Mountains foothill (Fig. 9b) than over the Great Plains where MCSs mature and grow to the maximum horizontal extent. The spatial patterns of deeper MCS convective feature ETH (e.g., $ETH > 9$ km) correspond to the region with frequent occurrence of significant hail echoes (reflectivity > 60 dBZ) and fastest daytime growth of convection east of the Rocky Mountain foothill and the Great Plains (Fabry et al. 2017) (their Figs. 2c and 5b), suggesting that this region with fast growing intense deep convection during local summer afternoon also favors upscale growth of convection into MCSs. While the MCS PF sizes are similar between spring and fall, spring MCSs are generally more organized and more intense, as seen by the larger and deeper convective features over the Great Plains and the SE. The SGP typically has deeper convective features in the spring than the NGP, although their convective feature diameters are comparable. Winter MCSs have the smallest and shallowest convective features; only convection near the SE is able to reach 5–6 km MSL on average for the 20-dBZ ETH.

One of the advantages of tracking MCSs throughout their life cycles using a mosaic radar dataset covering a

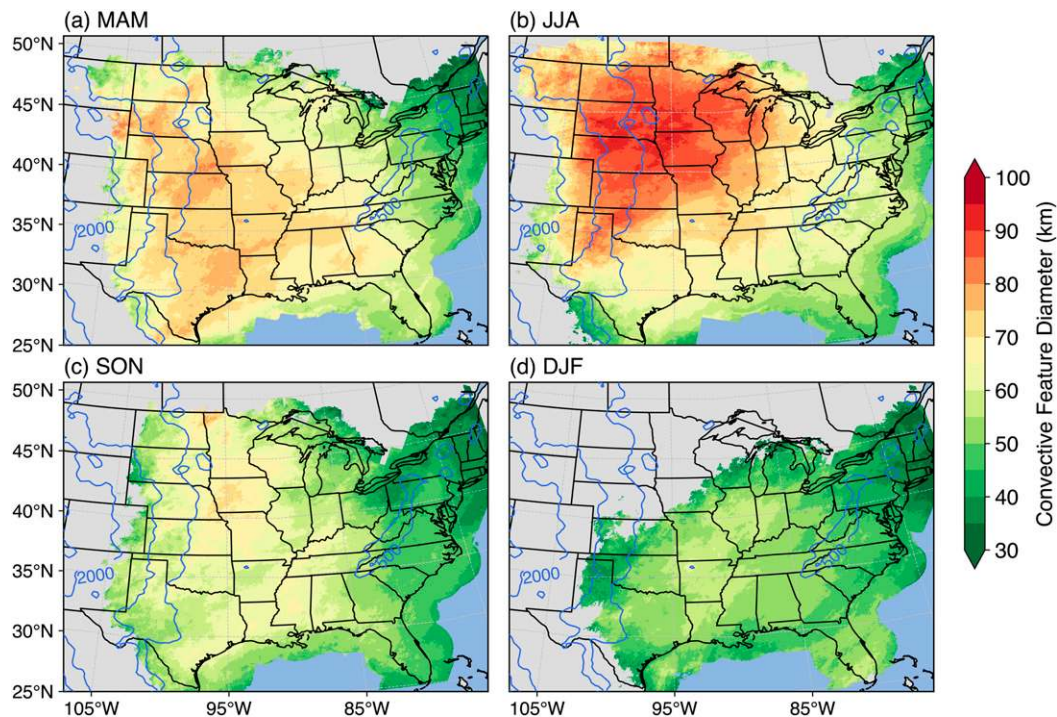


FIG. 15. As in Fig. 14, but for the average MCS largest convective feature equivalent diameter. Terrain heights are in blue contours (500, 1000, and 2000 m).

large region is that we can examine the evolution of their 3D characteristics from initial convective initiation through dissipation. Given the wide variety of MCS lifetimes, we composited MCSs in the same region and season following Feng et al. (2018), by normalizing the MCS lifetime to a relative time between hour 0 and 20, where hour 0 denotes convective initiation and hour 20 denotes dissipation. Six key parameters describing the horizontal and vertical MCSs characteristics during spring and summer are shown in Fig. 17: upper-level CCS area, volumetric rainfall (i.e., total rainfall integrated within an MCS), convective rain area, stratiform rain area, 40-dBZ convective ETH, and mean rain rate (averaged over all PFs within an MCS). CCS area and volumetric rainfall reflect the MCS horizontal dimensions. Convective and stratiform rain areas are closely related to precipitation amount in the respective areas; 40-dBZ convective ETH and mean rain rate are proxies of MCS intensity.

Interesting contrasts between the spring and summer seasons, as well as among the three subregions, are observed in the composite evolution. Compared to summer, MCSs during spring are significantly larger and produce more volumetric rainfall for all subregions. The NGP MCSs have the largest CCS during both seasons, followed by the SE during spring, while the SGP MCSs

are similar to the SE during summer (Figs. 17a,b). Different from CCS area, the SE MCSs are rainiest during spring, followed by the NGP and the SGP. During summer, the NGP MCSs are rainier than those in the SE and the SGP (Figs. 17c,d). Stratiform rain is the primary contributor to the volumetric rainfall, as the stratiform rain area and volumetric rainfall both show a similar evolution (Figs. 17g,h). Convective rain areas are significantly smaller than stratiform rain areas, and the seasonal difference is rather small (Figs. 17e,f). The NGP has the largest convective rain area, followed by the SE and the SGP. Given similar convective rain area, MCSs with larger stratiform rain area imply a larger stratiform rainfall contribution to the total rainfall. Based on convection-permitting model simulations, more stratiform rainfall results in top-heavier diabatic heating profiles, which strengthen the mesoscale circulation of the MCS and promote a stronger upscale feedback to the large-scale environments (Yang et al. 2017; Feng et al. 2018). Observational evidence in this study suggests that the spring MCSs may have a stronger upscale feedback to the large-scale environments than MCSs during summer.

Convective intensities (Figs. 17i–l) evolve quite differently than MCS cloud and rainfall area. Convection associated with the NGP MCSs during summer is the

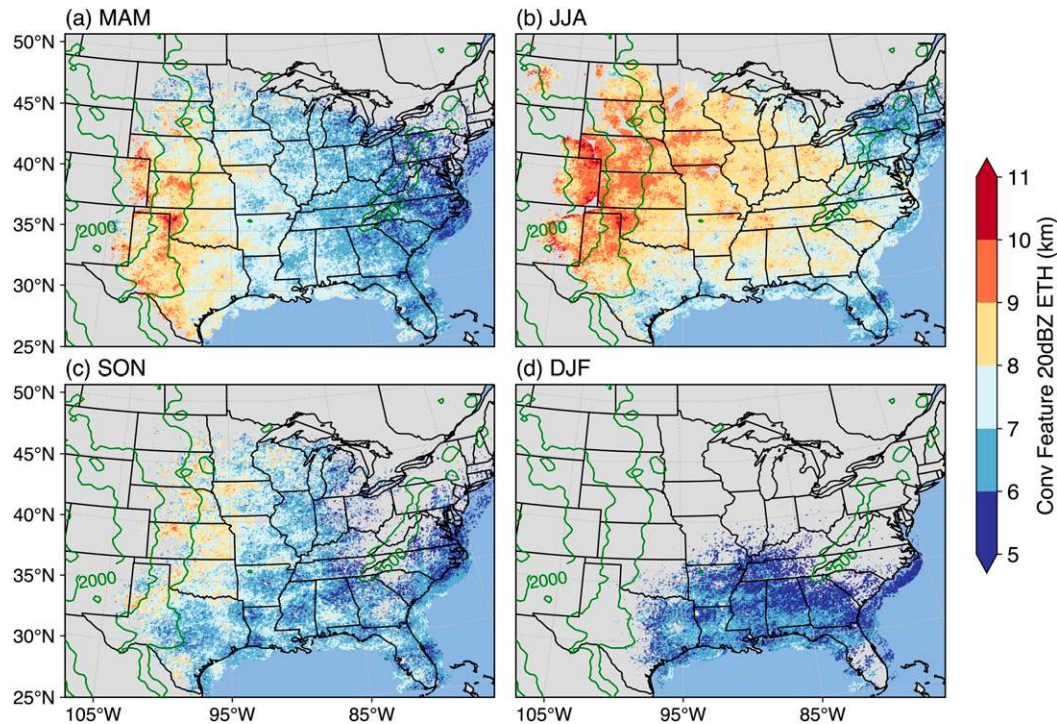


FIG. 16. As in Fig. 14, but for the average MCS largest convective feature 20-dBZ echo-top height. To ensure more accurate estimates of echo-top heights, only regions with typical vertical sampling distance from radars less than 1.25 km, minimum distance from the nearest radar less than 180 km, and covered by at least two radars are shown in this figure. Terrain heights are in green contours (500, 1000, and 2000 m).

deepest during the upscale growth stage (around hour 4, or 20% into the lifetime) and continues to show the strongest intensity throughout the mature and dissipating stages (Fig. 17j). During spring, the SGP MCSs show similar intensity with those in the NGP, while MCSs in the SE are the weakest among the subregions (Fig. 17i). Mean rain rate shows somewhat similar evolution to convective ETHs, albeit with a smaller decrease during the mature and dissipating stages (Figs. 17k,l). However, the regional contrasts in mean rain rate are different compared to the convective ETHs. This result demonstrates the value in characterizing MCS structures using 3D radar datasets as opposed to 2D precipitation datasets in previous studies (Prein et al. 2017a; Haberland and Ashley 2019). In particular, our finding suggests that using mean precipitation as a proxy for MCS intensity has limitations compared to using features derived from 3D radar-based characteristics.

7. Summary and conclusions

In this study, the spatiotemporal variability and 3D structures of MCSs east of the Rocky Mountains in the United States and the associated atmospheric large-scale environments across all seasons are characterized using

13 years of high-resolution observations. Long-lived and intense MCSs are objectively identified and tracked by applying the recently developed FLEXTRKR tracking algorithm (Feng et al. 2018) that uses three synthesized high-resolution datasets: merged geostationary satellite T_b , mosaic 3D NEXRAD radar reflectivity, and Stage IV precipitation. Atmospheric large-scale environments associated with MCSs are obtained from the NARR reanalysis dataset.

Long-lived and intense MCSs can occur in any season east of the Rocky Mountains, although different seasonal cycles are observed for three preferential subregions: NGP, SGP, and SE. Consistent with previous studies, we find MCSs are most frequent during spring and summer over the Great Plains and the MCSs account for well over 50% of total precipitation (some regions up to 70%) during the warm season (Figs. 2 and 3). MCSs are least frequent during fall, when they are primarily found in the Great Plains. Winter MCSs most commonly occur in the SE, contributing to over 40% of cold season total precipitation. MCSs in the Great Plains have the strongest seasonal cycle, peaking in May in the SGP and June in the NGP (Fig. 4). In contrast, MCSs in the SE have a weak seasonal cycle, although they are more frequent in July and December.

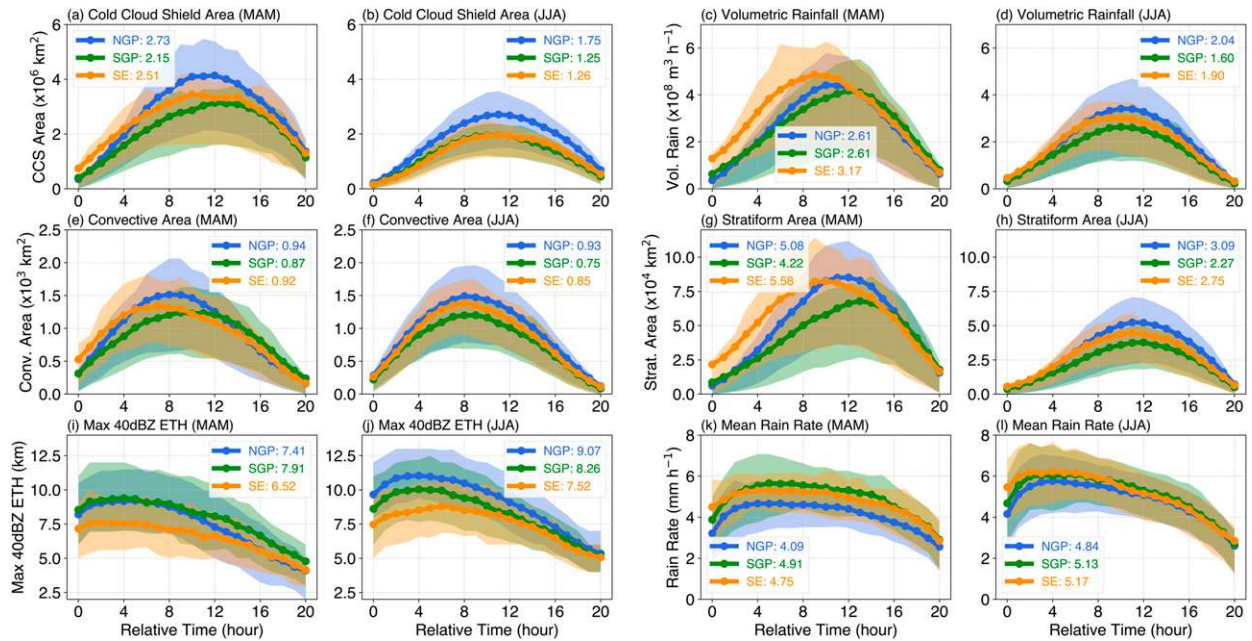


FIG. 17. Composite evolution of MCSs for the three subregions during spring and summer. (a),(b) Cold cloud shield area, (c),(d) volumetric rainfall, (e),(f) convective rain area, (g),(h) stratiform rain area, (i),(j) convective maximum 40-dBZ echo-top height, and (k),(l) mean rain rate. The x axis shows relative MCS time, where hour 0 denotes convective initiation and hour 20 denotes dissipation. Lines show the average values, and shadings denote the 25th and 75th percentile values at each time. Numbers in the legends are the average values across the MCS lifetime.

The key findings for the atmospheric large-scale environments, in terms of the associated MCS diurnal cycle and 3D characteristics, are summarized in Table 3. During spring and fall, composite MCS large-scale environments, diurnal cycle, and 3D characteristics share many similarities. MCSs commonly initiate ahead of a midlevel

trough associated with baroclinic waves (Fig. 5). Strong low-level convergence and upper-level divergence are observed over each subregion (Fig. 6). The Great Plains LLJ, likely enhanced by baroclinic waves, transports a large amount of moisture and instability into the subregions. MCS genesis during spring most frequently

TABLE 3. Summary of key atmospheric large-scale environments, associated MCS diurnal cycle characteristics, and 3D characteristics across four seasons.

	Atmospheric large-scale environments	MCS diurnal cycle characteristics	Key MCS 3D characteristics
Spring/fall	Strong baroclinic forcing + thermodynamics: ahead of midlevel trough, low-level convergence with upper-level divergence, strong LLJ advection causes anomalous moisture increases	Nocturnal maximum rainfall, convection not always surface triggered	Convective feature: large, deep Stratiform area: large Rain volume: high
Summer	Weak baroclinic forcing + favorable thermodynamics: high pressure ridge dominates, warm surface, high background low-level moisture	Strongest diurnal amplitude with nocturnal maximum rainfall, surface triggering dominates in the afternoon	Convective feature: largest, deepest Stratiform area: smallest Rain volume: low
Winter	Strong baroclinic forcing: strongest low-level convergence and upper-level divergence, largest moisture anomaly required to overcome weak thermodynamic support	Little to no diurnal variability	Convective feature: smallest, weakest Stratiform area: largest Rain volume: highest

occurs in the central Great Plains (Fig. 9a) around 1800–1900 LST (Fig. 10b), although a fraction of MCSs also initiate during nocturnal and morning hours (0000–0800 LST). MCS precipitation peaks around local midnight or early morning (Figs. 11a–c). Spring MCS convective features are both large and deep (Figs. 15a and 16a), along with large stratiform rain area and high total rainfall volume (Figs. 17c,g).

During summer, MCS large-scale environments and 3D characteristics are substantially different compared to spring and fall. MCSs commonly occur under or ahead of a high pressure ridge. The baroclinic forcing is the weakest among all seasons, denoted by weak low-level convergence and upper-level divergence (Figs. 5b,f,j and 6b,f,j). Mean low-level humidity is the highest among all seasons due to a warm surface. Strong diurnal heating at the Rocky Mountains foothills, or sea breeze convergence at the SE coastal region during the daytime, likely provides convective triggering mechanisms. MCS genesis during summer is concentrated just east of the Rocky Mountains Front Range and the coastal area of the SE (Fig. 9b). The majority of MCS genesis occurs at 1800 LST in the Great Plains and at 1300 LST in the SE (Fig. 10d). The strongest MCS precipitation diurnal cycle amplitude is observed from the Rocky Mountains foothills to the Great Plains (Figs. 11d,e). Summer MCS convective features are the largest and deepest among all seasons (Figs. 15b and 16b), but the stratiform rain area is the smallest with the lowest total rainfall volume (Figs. 17d,h).

Last, winter MCSs are characterized by the strongest baroclinic forcing and largest MCS PFs. Largest low-level convergence and moisture anomalies ahead of deep troughs over the SGP and SE are needed to overcome the weak thermodynamic support during the cold season (Figs. 5 and 6). Little to no MCS diurnal variability is observed across all regions (Fig. 10h). Winter MCS convective features are the smallest and weakest (Figs. 15d and 16d), but the stratiform rain area is the largest with the highest total rainfall volume (not shown).

This study shows that long-lived and intense MCSs are an important component of the hydrologic cycle east of the Rocky Mountains throughout the entire year, particularly during the warm seasons in the Great Plains and outside of the summer in the SE. Distinctly different atmospheric large-scale environments across the warm and cold seasons have significant impacts on the 3D structure of MCSs. Considering the combination of strong baroclinic forcing and favorable thermodynamic environments during spring and fall, simulation of MCSs during these transition seasons should be achievable for GCMs as long as the large-scale circulations are properly simulated, and the scale of triggering

mechanisms (e.g., dryline convergence) is resolved. In contrast, summer MCSs should be the most difficult for GCMs to simulate due to the associated weak baroclinic forcing and favorable thermodynamic environments, suggested by recent modeling studies (Prein et al. 2017a; Feng et al. 2018). Small-scale processes, such as diurnally driven turbulence and subtle convergence patterns in the lower troposphere, could serve as convective triggering mechanisms. Subsequent upscale growth into MCSs in the Great Plains is likely supported by subsynoptic-scale disturbances [e.g., midtropospheric shortwave perturbations associated with the Rocky Mountains, e.g., Wang et al. (2011b)] that coincide with sufficient moisture and instability provided by a nocturnal LLJ. Furthermore, land surface impact such as soil moisture feedbacks, boundary layer turbulence, and cloud radiative feedbacks, could play more important roles during summer. A better understanding of the relative importance of these processes to MCS genesis and maintenance is needed as GCM development pushes toward higher resolution and more sophisticated physics parameterizations. Long-term high-resolution observational datasets such as the MCS database developed in this study will be important benchmarks for evaluating the performance of next-generation GCMs and weather forecasting models.

Acknowledgments. This study is mainly supported by the Climate Model Development and Validation activity funded by the Office of Biological and Environmental Research (BER) in the U.S. Department of Energy (DOE) Office of Science. Some data analysis and writing of the manuscript are also supported by the DOE Office of Science BER as part of the Regional and Global Modeling and Analysis program through the Water Cycle and Climate Extremes Modeling (WACCME) scientific focus area. C. Homeyer was funded by NSF Grant AGS-1522910. This research used computational resources from the National Energy Research Scientific Computing Center (NERSC), a DOE User Facility supported by the Office of Science under Contract DE-AC02-05CH11231. PNNL is operated for DOE by Battelle Memorial Institute under Contract DE-AC05-76RL01830. The Global Merged IR dataset is obtained at NASA Goddard Earth Sciences Data and Information Services Center (<https://doi.org/10.5067/P4HZB9N27EKU>), the GridRad radar dataset is obtained from the Research Data Archive of the National Center for Atmospheric Research (NCAR) (<https://doi.org/10.5065/D6NK3CR7>), the Stage IV data are obtained from the NCAR Earth Observing Laboratory (<https://data.eol.ucar.edu/dataset/21.093>), and the NARR dataset is obtained from NOAA Earth System Research Laboratory Physical Science Division

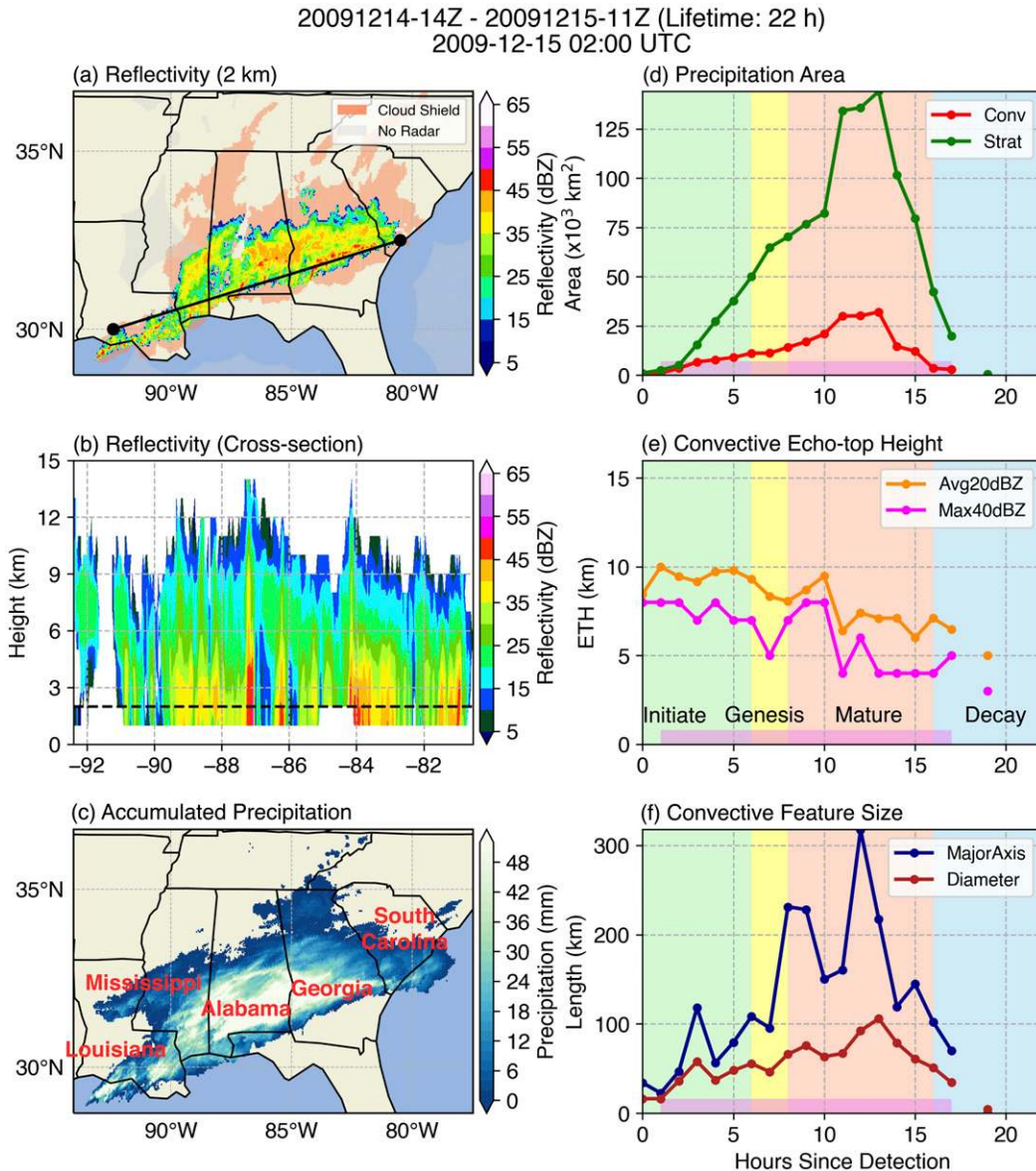


FIG. A1. As in Fig. 1, but for a winter MCS case in the southeast United States.

(<https://www.esrl.noaa.gov/psd/data/narr/>). The MCS dataset developed in this study will be available in the DOE Atmospheric Radiation Measurement (ARM) Research Facility website upon publication of the paper.

APPENDIX

An Example of Winter MCS

Figure A1 shows an example of a winter MCS in the Southeast. While equally long-lived (22 h) and at times reaching substantially larger horizontal dimension than the summer MCS case (Fig. 1), the winter MCS shows

drastically different 3D characteristics. Although the largest convective feature did reach 100 km in length, the 40-dBZ convective ETH is significantly shallower than the summer MCS case. This MCS was supported by a synoptic-scale baroclinic trough extending from the middle to upper troposphere, with a low-level low pressure center moving across the central Plains. Isolated convection was first triggered along a surface warm front transporting warm and humid air from the Gulf of Mexico into the coastal region of Louisiana. As the cold front associated with the low pressure system approached the southeast region with tightened pressure gradient and enhanced frontogenesis, a line of convection with embedded echoes

exceeding 45 dBZ formed along the frontal boundary. The convective cells were continuously advected north-eastward by the low-level winds, forming a broad stratiform rain area as old convective cells decay. Although the winter MCS formed in a background large-scale environment substantially different from the summer case, radar data show that the MCS is convective in nature, which is different from broad stratiform precipitation that forms via frontal lifting mechanisms.

REFERENCES

- Ashley, W. S., and T. L. Mote, 2005: Derecho hazards in the United States. *Bull. Amer. Meteor. Soc.*, **86**, 1577–1592, <https://doi.org/10.1175/BAMS-86-11-1577>.
- , P. G. Dixon, S. L. Trotter, E. J. Powell, J. D. Durkee, and A. J. Grundstein, 2003: Distribution of mesoscale convective complex rainfall in the United States. *Mon. Wea. Rev.*, **131**, 3003–3017, [https://doi.org/10.1175/1520-0493\(2003\)131<3003:DOMCCR>2.0.CO;2](https://doi.org/10.1175/1520-0493(2003)131<3003:DOMCCR>2.0.CO;2).
- Balling, R. C., 1985: Warm season nocturnal precipitation in the Great Plains of the United States. *J. Climate Appl. Meteor.*, **24**, 1383–1387, [https://doi.org/10.1175/1520-0450\(1985\)024<1383:WSNPIT>2.0.CO;2](https://doi.org/10.1175/1520-0450(1985)024<1383:WSNPIT>2.0.CO;2).
- Ban, N., J. Schmidli, and C. Schär, 2014: Evaluation of the convection-resolving regional climate modeling approach in decade-long simulations. *J. Geophys. Res. Atmos.*, **119**, 7889–7907, <https://doi.org/10.1002/2014JD021478>.
- Bentley, M. L., and J. A. Sparks, 2003: A 15 yr climatology of derecho-producing mesoscale convective systems over the central and eastern United States. *Climate Res.*, **24**, 129–139, <https://doi.org/10.3354/cr024129>.
- Bowman, K. P., and C. R. Homeyer, 2017: GridRad—Three-Dimensional Gridded NEXRAD WSR-88D Radar Data. Computational and Information Systems Laboratory, NCAR, accessed 1 October 2017, <https://doi.org/10.5065/D6NK3CR7>.
- Carbone, R. E., and J. D. Tuttle, 2008: Rainfall occurrence in the U.S. warm season: The diurnal cycle. *J. Climate*, **21**, 4132–4146, <https://doi.org/10.1175/2008JCLI2275.1>.
- , J. W. Conway, N. A. Crook, and M. W. Moncrieff, 1990: The generation and propagation of a nocturnal squall line. Part I: Observations and implications for mesoscale predictability. *Mon. Wea. Rev.*, **118**, 26–49, [https://doi.org/10.1175/1520-0493\(1990\)118<0026:TGAPOA>2.0.CO;2](https://doi.org/10.1175/1520-0493(1990)118<0026:TGAPOA>2.0.CO;2).
- , J. D. Tuttle, D. A. Ahijevych, and S. B. Trier, 2002: Inferences of predictability associated with warm season precipitation episodes. *J. Atmos. Sci.*, **59**, 2033–2056, [https://doi.org/10.1175/1520-0469\(2002\)059<2033:IOPAWW>2.0.CO;2](https://doi.org/10.1175/1520-0469(2002)059<2033:IOPAWW>2.0.CO;2).
- Chan, S. C., E. J. Kendon, H. J. Fowler, S. Blenkinsop, N. M. Roberts, and C. A. T. Ferro, 2014: The value of high-resolution Met Office regional climate models in the simulation of multihourly precipitation extremes. *J. Climate*, **27**, 6155–6174, <https://doi.org/10.1175/JCLI-D-13-00723.1>.
- Chen, S. S., and W. M. Frank, 1993: A numerical study of the genesis of extratropical convective mesovortices. Part I: Evolution and dynamics. *J. Atmos. Sci.*, **50**, 2401–2426, [https://doi.org/10.1175/1520-0469\(1993\)050<2401:ANSOTG>2.0.CO;2](https://doi.org/10.1175/1520-0469(1993)050<2401:ANSOTG>2.0.CO;2).
- Coniglio, M. C., J. Y. Hwang, and D. J. Stensrud, 2010: Environmental factors in the upscale growth and longevity of MCSs derived from Rapid Update Cycle analyses. *Mon. Wea. Rev.*, **138**, 3514–3539, <https://doi.org/10.1175/2010MWR3233.1>.
- Dai, A., F. Giorgi, and K. E. Trenberth, 1999: Observed and model-simulated diurnal cycles of precipitation over the contiguous United States. *J. Geophys. Res.*, **104**, 6377–6402, <https://doi.org/10.1029/98JD02720>.
- Dee, D. P., and Coauthors, 2011: The ERA-Interim reanalysis: Configuration and performance of the data assimilation system. *Quart. J. Roy. Meteor. Soc.*, **137**, 553–597, <https://doi.org/10.1002/qj.828>.
- Doswell, C. A., H. E. Brooks, and R. A. Maddox, 1996: Flash flood forecasting: An ingredients-based methodology. *Wea. Forecasting*, **11**, 560–581, [https://doi.org/10.1175/1520-0434\(1996\)011<0560:FFFAIB>2.0.CO;2](https://doi.org/10.1175/1520-0434(1996)011<0560:FFFAIB>2.0.CO;2).
- Fabry, F., V. Meunier, B. P. Treserras, A. Cournoyer, and B. Nelson, 2017: On the climatological use of radar data mosaics: Possibilities and challenges. *Bull. Amer. Meteor. Soc.*, **98**, 2135–2148, <https://doi.org/10.1175/BAMS-D-15-00256.1>.
- Fan, J. W., and Coauthors, 2017: Cloud-resolving model inter-comparison of an MC3E squall line case: Part I—Convective updrafts. *J. Geophys. Res. Atmos.*, **122**, 9351–9378, <https://doi.org/10.1002/2017JD026622>.
- Feng, Z., X. Q. Dong, B. K. Xi, C. Schumacher, P. Minnis, and M. Khaiyer, 2011: Top-of-atmosphere radiation budget of convective core/stratiform rain and anvil clouds from deep convective systems. *J. Geophys. Res.*, **116**, D23202, <https://doi.org/10.1029/2011JD016451>.
- , L. R. Leung, S. Hagos, R. A. Houze, C. D. Burleyson, and K. Balaguru, 2016: More frequent intense and long-lived storms dominate the springtime trend in central US rainfall. *Nat. Commun.*, **7**, 13429, <https://doi.org/10.1038/ncomms13429>.
- , R. A. Houze Jr., S. Hagos, J. Hardin, Q. Yang, B. Han, and J. Fan, 2018: Structure and evolution of mesoscale convective systems: Sensitivity to cloud microphysics in convection-permitting simulations over the United States. *J. Adv. Model. Earth Syst.*, **10**, 1470–1494, <https://doi.org/10.1029/2018MS001305>.
- Fritsch, J. M., R. J. Kane, and C. R. Chelius, 1986: The contribution of mesoscale convective weather systems to the warm-season precipitation in the United States. *J. Climate Appl. Meteor.*, **25**, 1333–1345, [https://doi.org/10.1175/1520-0450\(1986\)025<1333:TCOMCW>2.0.CO;2](https://doi.org/10.1175/1520-0450(1986)025<1333:TCOMCW>2.0.CO;2).
- , J. D. Murphy, and J. S. Kain, 1994: Warm core vortex amplification over land. *J. Atmos. Sci.*, **51**, 1780–1807, [https://doi.org/10.1175/1520-0469\(1994\)051<1780:WCVAOL>2.0.CO;2](https://doi.org/10.1175/1520-0469(1994)051<1780:WCVAOL>2.0.CO;2).
- Fujita, T., 1958: Structure and movement of a dry front. *Bull. Amer. Meteor. Soc.*, **39**, 574–582, <https://doi.org/10.1175/1520-0477-39.11.574>.
- Gao, Y., L. R. Leung, C. Zhao, and S. Hagos, 2017: Sensitivity of U.S. summer precipitation to model resolution and convective parameterizations across gray zone resolutions. *J. Geophys. Res. Atmos.*, **122**, 2714–2733, <https://doi.org/10.1002/2016JD025896>.
- Geerts, B., 1998: Mesoscale convective systems in the southeast United States during 1994–95: A survey. *Wea. Forecasting*, **13**, 860–869, [https://doi.org/10.1175/1520-0434\(1998\)013<0860:MCSITS>2.0.CO;2](https://doi.org/10.1175/1520-0434(1998)013<0860:MCSITS>2.0.CO;2).
- , and Coauthors, 2017: The 2015 Plains Elevated Convection at Night field project. *Bull. Amer. Meteor. Soc.*, **98**, 767–786, <https://doi.org/10.1175/BAMS-D-15-00257.1>.
- Gustafson, W. I., P.-L. Ma, and B. Singh, 2014: Precipitation characteristics of CAM5 physics at mesoscale resolution during MC3E and the impact of convective timescale choice. *J. Adv. Model. Earth Syst.*, **6**, 1271–1287, <https://doi.org/10.1002/2014MS000334>.
- Haberlie, A. M., and W. S. Ashley, 2019: A radar-based climatology of mesoscale convective systems in the United States.

- J. Climate*, **32**, 1591–1606, <https://doi.org/10.1175/JCLI-D-18-0559.1>.
- Higgins, R. W., Y. Yao, and X. L. Wang, 1997: Influence of the North American monsoon system on the U.S. summer precipitation regime. *J. Climate*, **10**, 2600–2622, [https://doi.org/10.1175/1520-0442\(1997\)010<2600:IOTNAM>2.0.CO;2](https://doi.org/10.1175/1520-0442(1997)010<2600:IOTNAM>2.0.CO;2).
- Hoch, J., and P. Markowski, 2005: A climatology of springtime dryline position in the U.S. Great Plains region. *J. Climate*, **18**, 2132–2137, <https://doi.org/10.1175/JCLI3392.1>.
- Homeyer, C. R., and K. P. Bowman, 2017: Algorithm Description Document for Version 3.1 of the Three-Dimensional Gridded NEXRAD WSR-88D Radar (GridRad) Dataset. Tech. Rep., 23 pp.
- Houze, R. A., 2004: Mesoscale convective systems. *Rev. Geophys.*, **42**, RG4003, <https://doi.org/10.1029/2004RG000150>.
- , 2018: 100 years of research on mesoscale convective systems. *A Century of Progress in Atmospheric and Related Sciences: Celebrating the American Meteorological Society Centennial*, Meteor. Monogr., No. 59, Amer. Meteor. Soc., 17.11–17.54, <https://doi.org/10.1175/AMSMONOGRAPHS-D-18-0001.1>.
- , B. F. Smull, and P. Dodge, 1990: Mesoscale organization of springtime rainstorms in Oklahoma. *Mon. Wea. Rev.*, **118**, 613–654, [https://doi.org/10.1175/1520-0493\(1990\)118<0613:MOOSRI>2.0.CO;2](https://doi.org/10.1175/1520-0493(1990)118<0613:MOOSRI>2.0.CO;2).
- Janowiak, J. E., R. J. Joyce, and Y. Yarosh, 2001: A real-time global half-hourly pixel-resolution infrared dataset and its applications. *Bull. Amer. Meteor. Soc.*, **82**, 205–218, [https://doi.org/10.1175/1520-0477\(2001\)082<0205:ARTGHH>2.3.CO;2](https://doi.org/10.1175/1520-0477(2001)082<0205:ARTGHH>2.3.CO;2).
- Jiang, X., N.-C. Lau, and S. A. Klein, 2006: Role of eastward propagating convection systems in the diurnal cycle and seasonal mean of summertime rainfall over the U.S. Great Plains. *Geophys. Res. Lett.*, **33**, L19809, <https://doi.org/10.1029/2006GL027022>.
- Kendon, E. J., N. M. Roberts, H. J. Fowler, M. J. Roberts, S. C. Chan, and C. A. Senior, 2014: Heavier summer downpours with climate change revealed by weather forecast resolution model. *Nat. Climate Change*, **4**, 570–576, <https://doi.org/10.1038/nclimate2258>.
- Klein, S. A., X. Jiang, J. Boyle, S. Malyshev, and S. Xie, 2006: Diagnosis of the summertime warm and dry bias over the U.S. Southern Great Plains in the GFDL climate model using a weather forecasting approach. *Geophys. Res. Lett.*, **33**, L18805, <https://doi.org/10.1029/2006GL027567>.
- Kunkel, K. E., D. R. Easterling, D. A. R. Kristovich, B. Gleason, L. Stoecker, and R. Smith, 2012: Meteorological causes of the secular variations in observed extreme precipitation events for the conterminous United States. *J. Hydrometeorol.*, **13**, 1131–1141, <https://doi.org/10.1175/JHM-D-11-0108.1>.
- Laing, A. G., and J. M. Fritsch, 1997: The global population of mesoscale convective complexes. *Quart. J. Roy. Meteor. Soc.*, **123**, 389–405, <https://doi.org/10.1002/qj.49712353807>.
- , and —, 2000: The large-scale environments of the global populations of mesoscale convective complexes. *Mon. Wea. Rev.*, **128**, 2756–2776, [https://doi.org/10.1175/1520-0493\(2000\)128<2756:TLSEOT>2.0.CO;2](https://doi.org/10.1175/1520-0493(2000)128<2756:TLSEOT>2.0.CO;2).
- Li, L. F., W. H. Li, and Y. Kushnir, 2012: Variation of the North Atlantic subtropical high western ridge and its implication to southeastern US summer precipitation. *Climate Dyn.*, **39**, 1401–1412, <https://doi.org/10.1007/s00382-011-1214-y>.
- Lin, Y., 2011: GCIP/EOP Surface: Precipitation NCEP/EMC 4KM Gridded Data (GRIB) Stage IV Data, version 1.0. UCAR/NCAR, Earth Observing Laboratory, accessed 31 March 2016, <https://doi.org/10.5065/D6PG1QDD>.
- , W. Dong, M. Zhang, Y. Xie, W. Xue, J. Huang, and Y. Luo, 2017: Causes of model dry and warm bias over central U.S. and impact on climate projections. *Nat. Commun.*, **8**, 881, <https://doi.org/10.1038/s41467-017-01040-2>.
- Mesinger, F., and Coauthors, 2006: North American Regional Reanalysis. *Bull. Amer. Meteor. Soc.*, **87**, 343–360, <https://doi.org/10.1175/BAMS-87-3-343>.
- Moncrieff, M. W., 1992: Organized convective systems: Archetypal dynamical models, mass and momentum flux theory, and parameterization. *Quart. J. Roy. Meteor. Soc.*, **118**, 819–850, <https://doi.org/10.1002/qj.49711850703>.
- Morcrette, C. J., and Coauthors, 2018: Introduction to CAUSES: Description of weather and climate models and their near-surface temperature errors in 5 day hindcasts near the southern Great Plains. *J. Geophys. Res. Atmos.*, **123**, 2655–2683, <https://doi.org/10.1002/2017JD027199>.
- Nesbitt, S. W., R. Cifelli, and S. A. Rutledge, 2006: Storm morphology and rainfall characteristics of TRMM precipitation features. *Mon. Wea. Rev.*, **134**, 2702–2721, <https://doi.org/10.1175/MWR3200.1>.
- Parker, M. D., and R. H. Johnson, 2000: Organizational modes of midlatitude mesoscale convective systems. *Mon. Wea. Rev.*, **128**, 3413–3436, [https://doi.org/10.1175/1520-0493\(2001\)129<3413:OMOMMC>2.0.CO;2](https://doi.org/10.1175/1520-0493(2001)129<3413:OMOMMC>2.0.CO;2).
- Pinto, J. O., J. A. Grim, and M. Steiner, 2015: Assessment of the High-Resolution Rapid Refresh model's ability to predict mesoscale convective systems using object-based evaluation. *Wea. Forecasting*, **30**, 892–913, <https://doi.org/10.1175/WAF-D-14-00118.1>.
- Prein, A. F., C. Liu, K. Ikeda, R. Bullock, R. M. Rasmussen, G. J. Holland, and M. Clark, 2017a: Simulating North American mesoscale convective systems with a convection-permitting climate model. *Climate Dyn.*, <https://doi.org/10.1007/S00382-017-3993-2>.
- , —, —, S. B. Trier, R. M. Rasmussen, G. J. Holland, and M. P. Clark, 2017b: Increased rainfall volume from future convective storms in the US. *Nat. Climate Change*, **7**, 880–884, <https://doi.org/10.1038/S41558-017-0007-7>.
- Rickenbach, T. M., R. Nieto-Ferreira, C. Zarzar, and B. Nelson, 2015: A seasonal and diurnal climatology of precipitation organization in the southeastern United States. *Quart. J. Roy. Meteor. Soc.*, **141**, 1938–1956, <https://doi.org/10.1002/qj.2500>.
- Schaefer, J. T., 1974: The life cycle of the dryline. *J. Appl. Meteor.*, **13**, 444–449, [https://doi.org/10.1175/1520-0450\(1974\)013<0444:TLCOTD>2.0.CO;2](https://doi.org/10.1175/1520-0450(1974)013<0444:TLCOTD>2.0.CO;2).
- Schumacher, C., and R. A. Houze, 2003: Stratiform rain in the tropics as seen by the TRMM precipitation radar. *J. Climate*, **16**, 1739–1756, [https://doi.org/10.1175/1520-0442\(2003\)016<1739:SRITTA>2.0.CO;2](https://doi.org/10.1175/1520-0442(2003)016<1739:SRITTA>2.0.CO;2).
- , —, and I. Kraucunas, 2004: The tropical dynamical response to latent heating estimates derived from the TRMM precipitation radar. *J. Atmos. Sci.*, **61**, 1341–1358, [https://doi.org/10.1175/1520-0469\(2004\)061<1341:TTDRTL>2.0.CO;2](https://doi.org/10.1175/1520-0469(2004)061<1341:TTDRTL>2.0.CO;2).
- Schumacher, R. S., and R. H. Johnson, 2006: Characteristics of U.S. extreme rain events during 1999–2003. *Wea. Forecasting*, **21**, 69–85, <https://doi.org/10.1175/WAF900.1>.
- Smith, B. T., R. L. Thompson, J. S. Grams, C. Broyles, and H. E. Brooks, 2012: Convective modes for significant severe thunderstorms in the contiguous United States. Part I: Storm classification and climatology. *Wea. Forecasting*, **27**, 1114–1135, <https://doi.org/10.1175/WAF-D-11-00115.1>.
- Song, F., Z. Feng, L. R. Leung, R. A. Houze, J. Wang, J. Hardin, and C. R. Homeyer, 2019: Contrasting spring and summer

- large-scale environments associated with mesoscale convective systems over the U.S. Great Plains. *J. Climate*, <https://doi.org/10.1175/JCLI-D-18-0839.1>, in press.
- Starzec, M., C. R. Homeyer, and G. L. Mullendore, 2017: Storm labeling in three dimensions (SL3D): A volumetric radar echo and dual-polarization updraft classification algorithm. *Mon. Wea. Rev.*, **145**, 1127–1145, <https://doi.org/10.1175/MWR-D-16-0089.1>.
- Stevenson, S. N., and R. S. Schumacher, 2014: A 10-year survey of extreme rainfall events in the central and eastern United States using gridded multisensor precipitation analyses. *Mon. Wea. Rev.*, **142**, 3147–3162, <https://doi.org/10.1175/MWR-D-13-00345.1>.
- Tripoli, G. J., and W. R. Cotton, 1989: Numerical study of an observed orogenic mesoscale convective system. Part 1: Simulated genesis and comparison with observations. *Mon. Wea. Rev.*, **117**, 273–304, [https://doi.org/10.1175/1520-0493\(1989\)117<0273:NSOAOO>2.0.CO;2](https://doi.org/10.1175/1520-0493(1989)117<0273:NSOAOO>2.0.CO;2).
- Tuttle, J. D., and C. A. Davis, 2006: Corridors of warm season precipitation in the central United States. *Mon. Wea. Rev.*, **134**, 2297–2317, <https://doi.org/10.1175/MWR3188.1>.
- Van Weverberg, K., and Coauthors, 2018: CAUSES: Attribution of surface radiation biases in NWP and climate models near the U.S. southern Great Plains. *J. Geophys. Res. Atmos.*, **123**, 3612–3644, <https://doi.org/10.1002/2017JD027188>.
- Varble, A., and Coauthors, 2014: Evaluation of cloud-resolving and limited area model intercomparison simulations using TWP-ICE observations: 1. Deep convective updraft properties. *J. Geophys. Res. Atmos.*, **119**, 13 891–13 918, <https://doi.org/10.1002/2013JD021371>.
- Virts, K. S., and R. A. Houze, 2015: Variation of lightning and convective rain fraction in mesoscale convective systems of the MJO. *J. Atmos. Sci.*, **72**, 1932–1944, <https://doi.org/10.1175/JAS-D-14-0201.1>.
- Wallace, J. M., 1975: Diurnal variations in precipitation and thunderstorm frequency over the conterminous United States. *Mon. Wea. Rev.*, **103**, 406–419, [https://doi.org/10.1175/1520-0493\(1975\)103<0406:DVIPAT>2.0.CO;2](https://doi.org/10.1175/1520-0493(1975)103<0406:DVIPAT>2.0.CO;2).
- Wang, S.-Y., T.-C. Chen, and J. Correia, 2011a: Climatology of summer midtropospheric perturbations in the U.S. northern plains. Part I: Influence on northwest flow severe weather outbreaks. *Climate Dyn.*, **36**, 793–810, <https://doi.org/10.1007/s00382-009-0696-3>.
- , —, and E. S. Takle, 2011b: Climatology of summer midtropospheric perturbations in the U.S. northern plains. Part II: Large-scale effects of the Rocky Mountains on genesis. *Climate Dyn.*, **36**, 1221–1237, <https://doi.org/10.1007/s00382-010-0765-7>.
- Yang, Q., R. A. Houze, L. R. Leung, and Z. Feng, 2017: Environments of long-lived mesoscale convective systems over the central United States in convection permitting climate simulations. *J. Geophys. Res. Atmos.*, **122**, 13 288–13 307, <https://doi.org/10.1002/2017JD027033>.
- Yuan, J., and R. A. Houze, 2010: Global variability of mesoscale convective system anvil structure from A-Train satellite data. *J. Climate*, **23**, 5864–5888, <https://doi.org/10.1175/2010JCLI3671.1>.
- Ziegler, C. L., T. J. Lee, and R. A. Pielke, 1997: Convective initiation at the dryline: A modeling study. *Mon. Wea. Rev.*, **125**, 1001–1026, [https://doi.org/10.1175/1520-0493\(1997\)125<1001:CIATDA>2.0.CO;2](https://doi.org/10.1175/1520-0493(1997)125<1001:CIATDA>2.0.CO;2).